



Tourmaline in the Passagem de Mariana gold deposit (Brazil) revisited: major-element, trace-element and B-isotope constraints on metallogenesis

R. B. Trumbull¹ · G. M. Garda² · R. P. Xavier³ · J. A. D. Cavalcanti⁴ · M. S. Codeço¹

Received: 2 November 2017 / Accepted: 11 June 2018 / Published online: 25 June 2018
© Springer-Verlag GmbH Germany, part of Springer Nature 2018

Abstract

Tourmaline at Passagem de Mariana forms three associations: stratiform tourmalinite (T1), wall-rock alteration around quartz-sulfide veins (T2), and clusters within the veins (T3). The major-element composition of tourmaline is similar in all, with Mg/(Mg+Fe) from 0.59 to 0.83 (mean 0.69 ± 0.03) and total Al contents from 6.2 to 6.6 atoms per formula unit (apfu). The Y-site Al (0.2–0.6 apfu) is charge-balanced by the exchange $\text{NaMg}(\text{Al}\square)_{-1}$. Tourmalinite type (T1) is unzoned, whereas T2 and T3 grains display increasing Ti and Ca from core to rim. In situ trace-element analyses of T1 grains were prohibited by grain size and inclusions. The T2 and T3 tourmaline have similar trace-element values, except higher concentrations of Zn, Cu, and Co in T3, which is consistent with its location in the mineralized veins. The $\delta^{11}\text{B}$ values of T1 and T2 tourmaline range from -17.8 to -9.7‰ , with indistinguishable mean values (-13.9 ± 1.9 and $-13.8 \pm 1.6\text{‰}$, respectively), supporting field evidence that T1 tourmalinite is hydrothermal. The $\delta^{11}\text{B}$ values of T3 tourmaline are about 5‰ higher (mean $-8.9 \pm 1.3\text{‰}$), which we ascribe to depletion of ^{10}B in the vein fluid due to tourmalinization of wall rocks. This implies that the initial $\delta^{11}\text{B}$ value of hydrothermal fluid was about -11‰ (for 400 °C and the T1–T2 mean $\delta^{11}\text{B} = -14\text{‰}$). This indicates a crustal boron source but is otherwise non-specific. Based on geological arguments, we favor a source in the Minas Supergroup metasedimentary units hosting the deposit.

Keywords Gold deposits · Quadrilátero Ferrífero · Minas Gerais · Boron isotopes · Trace elements

Introduction

The Passagem de Mariana (PM) deposit is one of several auriferous deposits in the Ouro Preto region of the Quadrilátero Ferrífero (QF), where mineralization is closely associated with

tourmaline (Fig. 1). Since the first geological descriptions of the Passagem deposit in the 1800s, the spatial association of tourmalinite layers and tourmaline-rich lenses and breccias with auriferous quartz-carbonate-sulfide veins was noted and tourmaline was regarded as a proximity indicator for ore (e.g., Derby 1911). Most studies of the deposit, including these early works, considered it to be of epigenetic hydrothermal origin, whereas Fleischer and Routhier (1973) introduced a syngenetic model based largely on the interpretation of tourmalinites as primary features of boron-rich sedimentary protoliths. This syngenetic model for ore formation was contested by Barbosa et al. (1974) and more recent work has firmly established an epigenetic and hydrothermal origin for the mineralization at Passagem de Mariana and other gold deposits in the region, with a structural control related to thrust faults along the flanks of the Mariana anticline (e.g., Chauvet et al. 2001; Vial et al. 2007; Cabral et al. 2010). The tourmaline in the quartz veins formed during the mineralization event as shown by the common intergrowths with arsenopyrite, the main sulfide mineral in the deposit. The composition of tourmaline is clearly relevant to the mineralization event

Editorial handling: S.-Y. Jiang

Electronic supplementary material The online version of this article (<https://doi.org/10.1007/s00126-018-0819-z>) contains supplementary material, which is available to authorized users.

✉ R. B. Trumbull
bobby@gfz-potsdam.de

- ¹ GFZ German Research Centre for Geoscience, Telegrafenberg, Potsdam, Germany
- ² Instituto de Geociências, Universidade de São Paulo, São Paulo, Brazil
- ³ Instituto de Geociências, Universidade Estadual de Campinas (UNICAMP), Campinas, São Paulo, Brazil
- ⁴ Serviço Geológico do Brasil (CPRM), Belo Horizonte, MG, Brazil

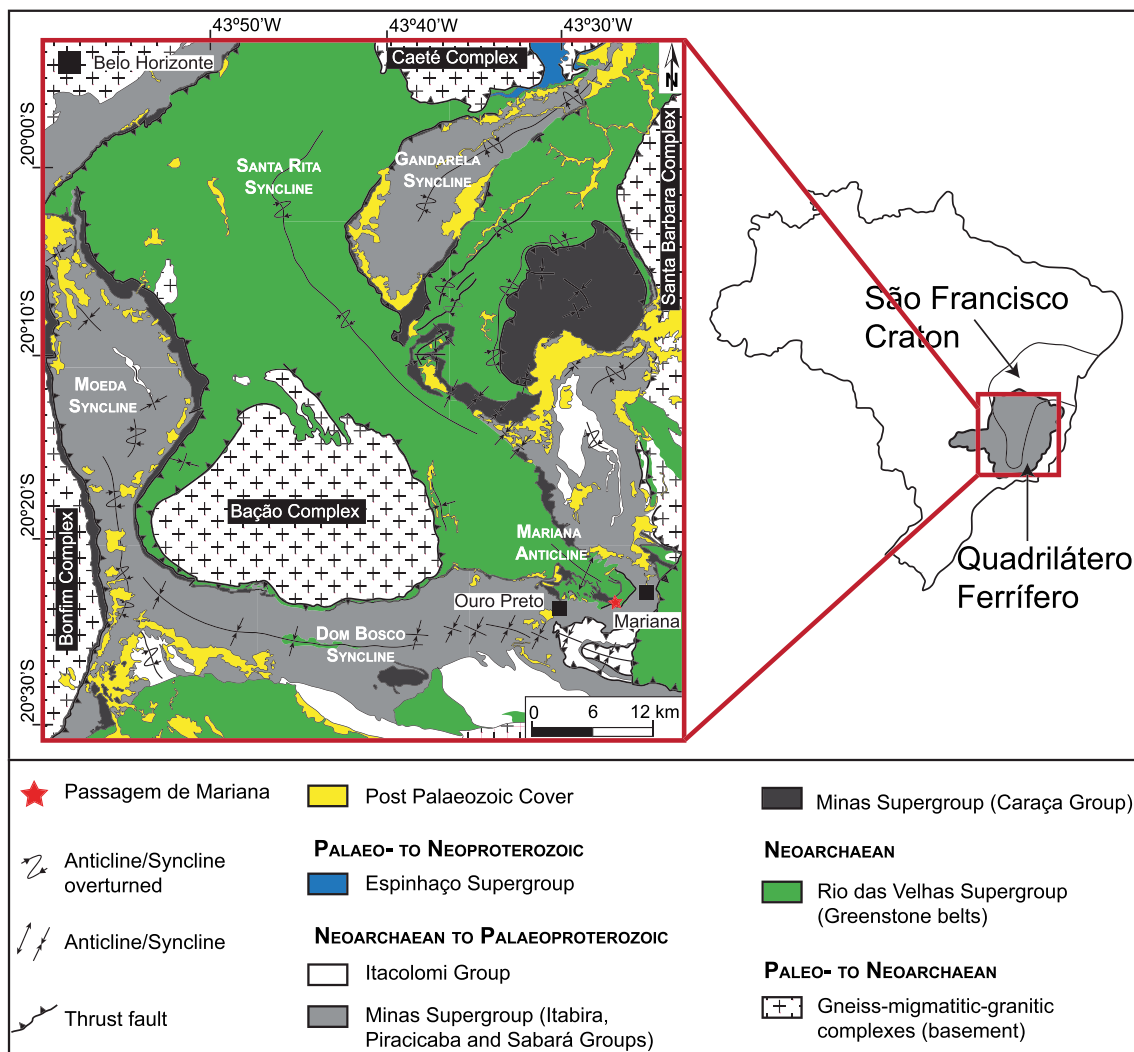


Fig. 1 Simplified geological map of the southern portion of Quadrilátero Ferrífero (Minas Gerais, Brazil) modified from Koglin et al. (2014) and Dorr (1969). The Passagem de Mariana mine is located in the SE corner of the map, marked by a star

and the aim of this paper is to integrate and jointly interpret major-element, trace-element, and B-isotope data of the tourmaline to constrain the source and composition of ore-bearing hydrothermal fluids.

We report results from in situ boron-isotope analyses by secondary ion mass spectrometry (SIMS) of tourmaline from selected samples reported in Cavalcanti and Xavier (2006) and Garda et al. (2009a). Some microprobe analyses were published in those reports, whereas other analyses were obtained for the SIMS study and are published here for the first time. The boron-isotope data were summarized in a conference abstract by Garda et al. (2010) but have not been published in full. Finally, we acquired in-situ trace-element data by laser ablation inductively coupled mass spectrometry (LA-ICP-MS) to complete the data set. Important context for the data and interpretations in this paper are given by B-isotope studies by Cabral et al. of other deposits in the region (Cabral et al. 2011, 2012a, b) and by Albert et al. (2018), who provide

tourmaline B-isotope data for late Archean granitic-pegmatitic intrusions, quartz veins, and wall rocks from the Bação dome in the NW of the study area (Fig. 1).

Geologic setting

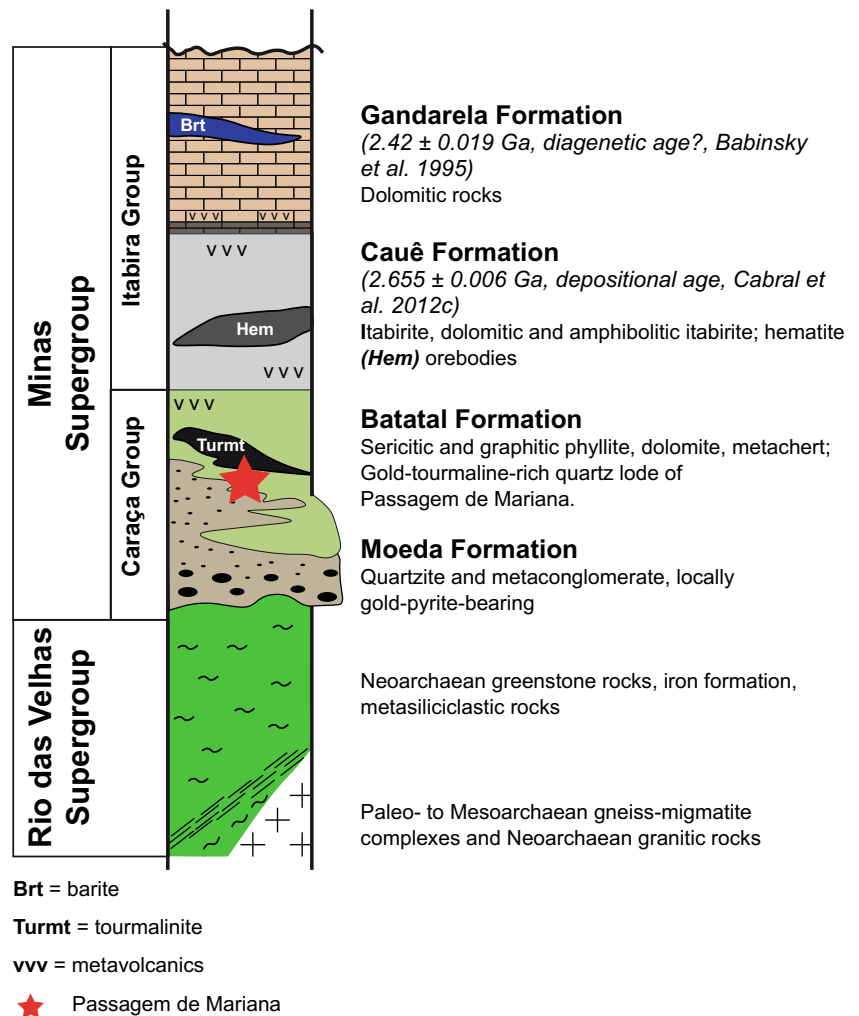
The Quadrilátero Ferrífero is a world class metallogenic province located in the southern border of the São Francisco craton (Fig. 1), from which gold has been one of the most economically important metals produced since the early eighteenth century. The Quadrilátero Ferrífero consists of an Archean granite-greenstone terrane and Neoproterozoic to Paleoproterozoic supracrustal sequences (Fig. 1). The basement rocks include gneiss and migmatite of trondhjemitic-tonalitic-granodioritic affinity with an age range of 3.38 to 2.90 Ga and late Archean calc-alkaline and anorogenic granite-gneiss complexes (e.g., Bação, Bonfim, and Caeté; Dorr 1969; Teixeira

et al. 1996; Alkmim and Marshak 1998; Farina et al. 2016). The Rio das Velhas Supergroup is a greenstone belt volcano-sedimentary sequence (2800–2740 Ma) composed, from base to top, by ultramafic (komatiite) and mafic (basaltic) volcanic rocks interlayered with chemical sedimentary rocks (iron formation), a felsic volcanoclastic-dominated unit, and an upper clastic unit, all of which are metamorphosed at greenschist to lower amphibolite facies (Baltazar and Zucchetti 2007). These rock units were commonly subjected to hydrothermal alteration and contain a significant number of formerly important and/or currently productive orogenic-type gold deposits (e.g., Morro Velho, Cuiabá, São Bento, Raposos, Córrego do Sítio), which are mostly confined to the basal mafic-ultramafic succession (Lobato et al. 2001). The Neoproterozoic and Proterozoic supracrustal sequences comprise the Minas (2.6–2.4 Ga) and Espinhaço (1.7 Ga) Supergroups and the Itacolomi Group (Dorr 1969; Machado et al. 1992; Klein and Ladeira 2000; Farina et al. 2016). The Minas Supergroup is most relevant to this study because it hosts the Passagem de Mariana deposit and others along the Mariana anticline. The Minas Supergroup is an approximately 6-km-thick sequence of low- to medium-

grade, clastic metasedimentary units unconformably deposited on the deformed Rio das Velhas Supergroup and overlain in turn by banded iron formation (itabirite) and dolomitic carbonates (Fig. 2). The lithostratigraphy of the Minas Basin suggests a continental shelf environment where terrestrial fluvial-lacustrine sediments were overlain by shallow marine chemical sediments and carbonates (e.g., Dorr, 1969; Farina et al. 2016, Dopico et al. 2017).

According to Alkmim and Marshak (1998), two sets of structures developed the tectonic architecture of the QF basement. The first set consists of northwest-verging folds and thrust faults that formed shortly after 2.12 Ga during the closure of a passive-margin basin, generating large asymmetric synclines (Dom Bosco, Moeda, Gandarela: Fig. 1). The second set comprises the prominent, dome-and-keel geometry in which troughs of deformed and metamorphosed supracrustal rocks surround basement granite-gneiss domes. A later tectonic event affecting this region was the Brasiliano/Panafrican orogeny in the Late Proterozoic to Early Cambrian, which is related to convergence of South America and Africa. The Brasiliano event (0.7–0.45 Ga) created a west-verging thrust

Fig. 2 Stratigraphic column of country rocks in the Mariana anticline, modified from Cabral and Koglin (2012). The section hosting the Passagem de Mariana deposit is indicated by a star



belt that reactivated and overprinted older structures within the QF. Shear zones were commonly developed at the contact between the supracrustal rocks and the basement complexes, and these are important hosts to gold mineralization at Passagem de Mariana and elsewhere in the QF.

The Passagem de Mariana deposit: geology and gold mineralization

The Passagem de Mariana gold deposit is 100 km southeast of Belo Horizonte in Minas Gerais State, Brazil. Together with many other gold deposits that are no longer mined, it forms part of a mineralized zone distributed along the southwest and southeast flanks of the Mariana anticline, which was affected by layer-parallel thrust faults along which the lode-gold deposits are localized (Fig. 1). The stratigraphic succession of the country rocks is shown in Fig. 2. The Minas Supergroup is the main host to the gold mineralization, and in the deposit area, it is represented by the Caraça Group that is conformably overlain by the Itabira Group. The Caraça Group is divided from base to top into the Moeda and Batatal formations. The Moeda Formation is mostly composed of quartzite, metaconglomerate (locally gold-pyrite bearing), and phyllite, whereas sericite phyllite, locally graphitic, as well as minor metachert and carbonate make up the Batatal Formation (Dorr 1969; Koglin et al. 2014). The Itabira Group is divided into the lower Cauê Formation, a more than 350-m-thick Lake Superior-type banded iron formation known as itabirite, and the overlying Gandarela Formation. The latter is an approximately 600-m-thick sequence of locally stromatolitic dolomite, limestone, graphitic phyllite, and dolomitic iron-rich rocks (Fig. 2; Dorr 1969; Babinski et al. 1995; Klein and Ladeira 2000).

The PM deposit produced more than 60 t of gold from the start of mining in the late seventeenth century until mine closure in 1985. The average gold grade in mineralized quartz veins was about 8 g/t (Vial et al. 2007). Numerous lens-shaped orebodies were exploited from a zone that follows the thrust contact of the Cauê Formation in the hanging wall and metasedimentary rocks of the Batatal Formation in the footwall. This structural setting is also the main mineralized zone in several deposits of the Ouro Preto district (Chauvet et al. 2001). At Passagem de Mariana, the thrust contact constitutes a highly deformed ductile fault zone typically up to 5 m thick, exceptionally reaching 10 m, in which lenticular, gold-bearing, quartz-tourmaline-sulfide veins alternate with boudinaged metacarbonate, sericite phyllite, graphitic phyllite, and sericite quartzite (Fig. 3). Vial et al. (2007) provide a detailed description of the rock units and mineralization style from underground mapping and observations in the Fundação orebody, from which the samples for this study (also Cabral and Koglin 2012; Cabral and Zeh 2015) were collected (Fig. 3). Mineral

proportions in the quartz veins and lenses vary according to host lithology, but quartz typically forms more than 60 vol%, tourmaline reaches up to 10 vol%, and sulfide minerals up to 5 vol%. The predominant sulfide mineral is arsenopyrite, with which tourmaline is commonly intergrown (e.g., Fig. 4d, f). In their paragenetic sequence derived from studies of Passagem de Mariana and the nearby Morro Santana mines, Chauvet et al. (2001) place the formation of tourmaline in an early, syn-metamorphic stage with quartz and in a later vein-stage with quartz, arsenopyrite, pyrite, chalcopyrite, pyrrhotite, and sphalerite. Gold and several Bi-, Te-, and Sb-bearing ore minerals formed later still, occurring as crack-fillings in arsenopyrite. Vial et al. (2007) also described the gold in Passagem de Mariana as forming after arsenopyrite. However, Cabral et al. (2017) found millimeter-sized alluvial clusters of intergrown gold and tourmaline, suggesting at least some tourmaline growth continued to the point of gold deposition.

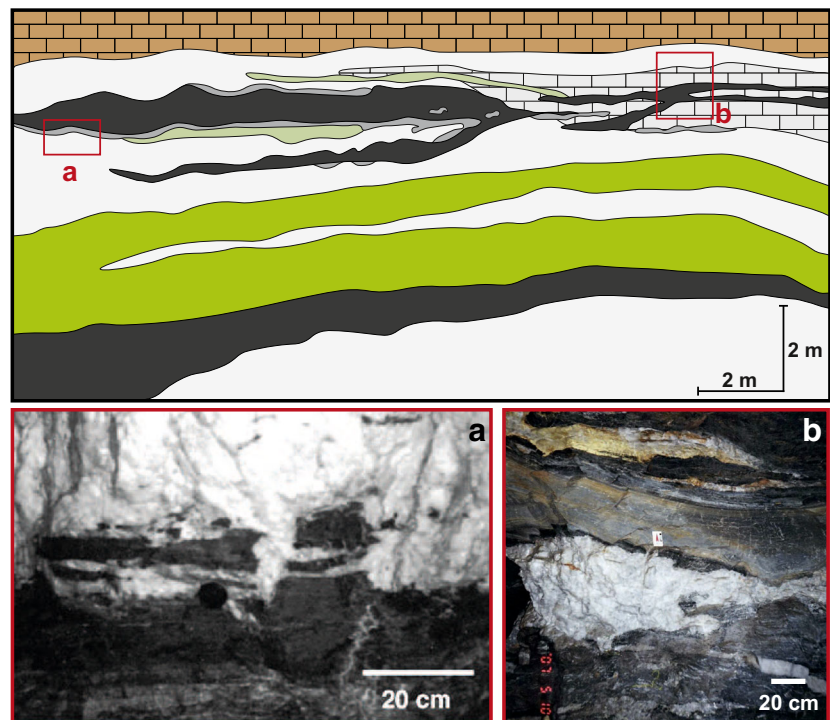
Although hosted by Archean to Proterozoic-age rocks of the Minas Supergroup, the age of mineralization at PM may be Cambrian, related to reactivation of older thrust faults during the Brasiliano event. This timing was suggested by Chauvet et al. (2001) based on early Paleozoic ^{40}Ar - ^{39}Ar ages (485 ± 4 Ma) of hydrothermal biotite and white mica from the PM and Morro de Santana deposits. Vial et al. (2007) suggested that the biotite age may have merely been reset during the Brasiliano event and not representative of mineralization. However, a concordant U-Pb date of 496 ± 2 Ma for xenotime in a tourmaline-rich vein in the PM deposit (Cabral and Zeh 2015) gives good evidence for a Cambrian age of gold mineralization.

Tourmaline occurrence in the deposit








Previous studies (e.g., Chauvet et al. 2001; Cavalcanti and Xavier 2006; Vial et al. 2007) established that tourmaline occurs in stratiform tourmalinite bands in mica-rich metaclastic rocks of the Batatal Formation, in alteration halos around the margins of quartz-carbonate-sulfide veins regardless of host lithology, and in the quartz veins themselves. Cavalcanti and Xavier (2006) distinguished them as types T1, T2, and T3, respectively, which we adopt in this paper:

- T1—stratiform tourmalinites: fine- to medium-grained, black layers from a few centimeters to 3-m-thick, containing up to 80 vol% tourmaline. The tourmalinites locally contain significant amounts of graphite (10–30 vol%) as well as minor quartz, apatite, rutile, titanite, and sulfide minerals (pyrite, arsenopyrite, chalcopyrite). Tourmalinite layers are concordant to the foliation of the enclosing rocks but are commonly disrupted as angular blocks or displaying boudinage in parallel with the pinch-and-swell structures of the quartz veins (Figs. 3a

Fig. 3 Geological sketch of level 315 of Fundão orebody, after Vial et al. (2007) with photos A and B showing the typical form of mineralized quartz veins with tourmalinite selvages exposed in mine pillars



Legend

	Dolomite itabirite (Cauê Formation)		Sericite phyllite and/or graphite-sericite phyllite (Batatal Fm)
	Quartz-carbonate-biotite-sericite schist (Batatal Fm)		Banded gray calcareous rock (Batatal Fm)
	Tourmalinite		Sericite quartzite (Moeda Fm)
	Gold-mineralized zones: milky quartz veins with tourmaline and sulfides		

and 4a). Although interpreted as pre-metamorphic by Cavalcanti and Xavier (2006) based on their stratiform, banded aspect, Vial et al. (2007) disputed a syngenetic origin because tourmalinites are restricted to the vicinity of quartz veins, because the tourmaline abundance in them increases with proximity to the veins and because oriented microstructures of mineral inclusions in T1 tourmaline requires that they grew after at least the first phase of deformation in the rocks.

- T2—tourmaline alteration occurs in zones up to 50-cm-thick in association with abundant sericite, biotite, and carbonate surrounding foliation-concordant and discordant quartz veins hosted in sericite-quartz phyllite, metacarbonate rocks, and graphitic phyllite. Type 2 tourmaline is medium- to coarse-grained and commonly color zoned, with pale green or tan cores and darker olive and brownish rims (Fig. 4c). Both concentric and patchy zoning patterns are observed (Fig. 4d). Locally, type 2 tourmaline crystals show comb structure, in which crystals project inward from the vein margin (Fig. 4f).

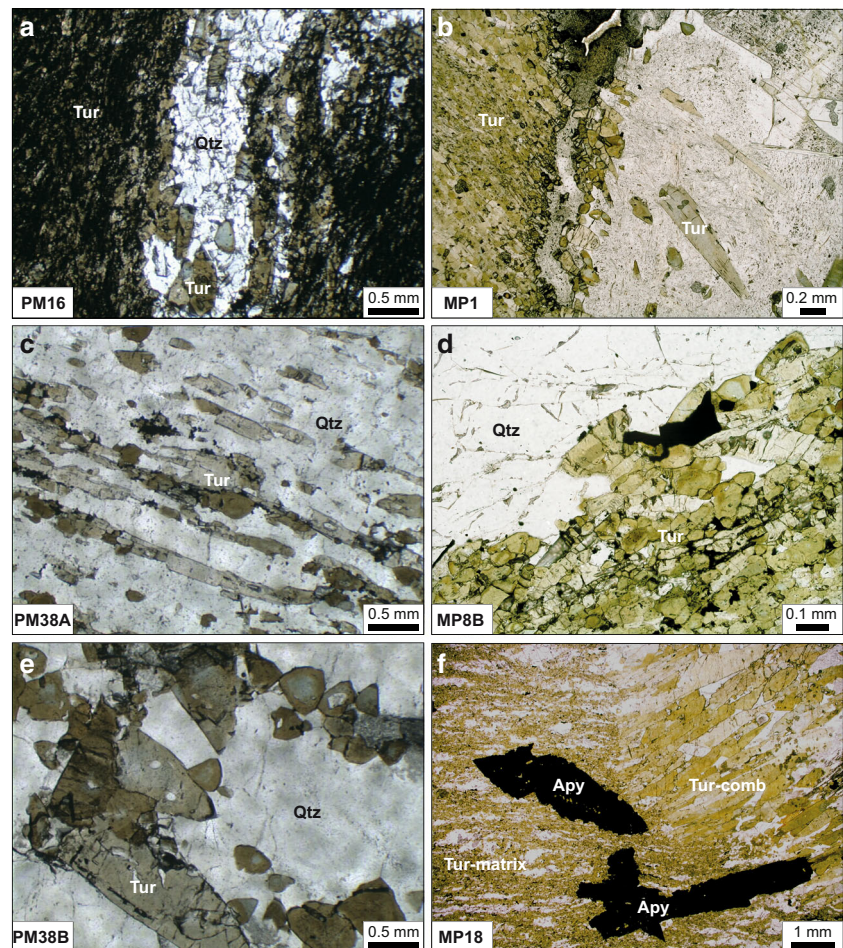
- T3—coarse-grained tourmaline clusters within mineralized quartz-sulfide veins (Fig. 4b, e). The tourmaline crystals are medium- to coarse-grained and color zoned like the type 2 tourmaline.

Materials and methods

The samples selected for this study are from sets of tourmaline samples described in Garda et al. (2009a: samples prefixed MP) and in Cavalcanti (2003: samples prefixed PM). All of the samples originate from underground workings in the Fundão orebody at levels 175, 265, and 315. The samples are assigned to the three tourmaline associations T1, T2, and T3 as follows:

- T1—tourmalinite:* PM16 (level 265), MP1 (level 175)
T2—alteration halo: PM33B (level 265), PM38A (level 265), and MP8B and MP18 (level 315)
T3—quartz veins: PM38B (level 265)

Fig. 4 Photomicrographs in transmitted light of thin sections illustrating three tourmaline types described in text. **a** T1 stratiform tourmaline (Tur) with quartz veinlet (Qtz): sample PM16. **b** T1 tourmalinite on the left, bordering a quartz vein containing zoned T3-type tourmaline: sample MP1. **c** T2 tourmaline intergrown with quartz at the edge of a mineralized vein, retaining the oriented fabric from wall rocks: sample PM38a. **d** T2 coarse, color-zoned tourmaline at the edge of mineralized quartz vein (opaque mineral is arsenopyrite): sample MP8B. **e** T3-type coarse, zoned tourmaline in mineralized quartz vein, sample PM38b. **f** T2 tourmaline at the edge of a mineralized quartz vein with two textural types: fine-grained matrix (Tur-matrix) and coarse-grained comb-texture growing into the vein (Tur-comb). The opaque mineral is arsenopyrite (Apy): sample MP18



Analytical techniques

The major-element composition of tourmaline described in this paper is based on a combined dataset of microprobe analyses reported by Garda et al. (2009a), Cavalcanti (2003), and Cabral and Koglin (2012) using the procedures described in the cited sources. Additional, previously unpublished data from RP Xavier were obtained at the GFZ Potsdam using a Cameca SX100 electron microprobe following procedures described in Trumbull et al. (2009). Different schemes to calculate mineral formulae from microprobe data were used in the original studies so we recalculated all data on the basis of 15 cations on the $X + Y + Z$ sites following the procedure of Henry et al. (2011). The recalculated compositions are reported in electronic supplementary material (ESM1) and a summary is given in Table 1. We note that some analyses from samples PM33B and PM38 yielded unreasonably low oxide totals (81–83 vs. 84–86 wt% for the other data sets). Examination of the analyses shows that most of the deficit is due to low SiO_2 and Al_2O_3 values which we attribute to an unrecognized calibration problem at the time of analysis. While unfortunate, the data are adequate for the purpose of tourmaline classification and for determining first-order

compositional parameters such as Mg# and the proportion of X-site vacancies.

The boron isotopic composition of tourmaline was determined with a Cameca IMS-6F instrument at GFZ in Potsdam. The thin sections used for microprobe analysis were re-polished with 1- μm alumina and distilled water to remove the carbon coat, then cleaned in an ultrasonic ethanol bath and coated with a $\sim 35\text{-nm}$ -thick, high-purity layer of gold. SIMS analyses employed a primary $^{16}\text{O}^-$ beam at nominal 12.5 kV and 0.8 nA focused to about 15 μm diameter on the sample surface. A 3-min preburn was used to remove the gold coating and establish steady sputtering conditions. A 150- μm diameter contrast aperture, 750- μm field aperture (equivalent to a 150- μm field of view), and an energy window of 50 V were used without voltage offset. The mass resolving power at these conditions was $M/\Delta M \approx 1430$, sufficient to separate the isobaric interference of $^{10}\text{B}^1\text{H}$ and ^{11}B . Each analysis consisted of 100 cycles at mass stations 10 and 11. The instrumental mass fractionation (IMF) and analytical quality were determined by repeated analyses of the tourmaline reference materials dravite (HS no. 108796) and schorl (HS no. 112566) from the Harvard Mineralogical Museum (Leeman and Tonerari 2001), whose compositions are similar to the PM

Table 1 Summary of tourmaline major-element compositions from electron microprobe analyses

Sample	Garda et al. (2009a)			Cavalcanti (2003)			This Study			Garda et al. (2009a)			This Study			This study						
	Ave. (n = 14) Unzoned MP-01 type 1	SD	Unzoned PM-16 type 1	Ave. (n = 9) Unzoned PM-16 type 1	SD	Unzoned PM-16 type 1	Ave. (n = 10) Unzoned PM-16 type 1	SD	Ave. (n = 7) Rim	SD	Ave. (n = 3) Unzoned MP-8b type 2	SD	Ave. (n = 7) Core	SD	Ave. (n = 8) Matrix MP-18 (type 2)	SD	Ave. (n = 6) Comb	SD	Ave. (n = 42)	SD	Ave. (n = 47)	SD
SiO ₂	36.70	0.27	36.53	0.29	33.92	1.23	36.60	0.30	36.83	0.18	36.42	0.27	36.60	0.30	36.81	0.66	36.29	1.05	34.77	0.57	34.25	0.59
Al ₂ O ₃	32.56	0.64	33.03	0.47	31.22	1.02	33.21	0.39	33.81	0.40	33.04	0.72	33.21	0.39	33.78	0.82	33.24	0.76	31.91	0.62	31.79	0.51
K ₂ O	0.02	0.01	0.01	0.01	0.02	0.01	0.01	0.01	0.02	0.01	0.02	0.01	0.01	0.01	0.02	0.01	0.01	0.01	0.02	0.01	0.02	0.01
TiO ₂	0.53	0.19	0.62	0.14	0.74	0.10	0.59	0.11	0.20	0.07	0.63	0.31	0.59	0.11	0.33	0.19	0.56	0.29	0.60	0.18	0.53	0.20
CaO	0.54	0.19	1.01	0.15	1.13	0.09	0.92	0.13	0.51	0.05	1.03	0.39	0.92	0.13	0.64	0.24	0.84	0.22	0.94	0.25	0.89	0.26
Cr ₂ O ₃	0.04	0.03	0.05	0.03	0.04	0.02	0.18	0.11	0.24	0.20	0.18	0.11	0.24	0.20	0.11	0.11	0.11	0.11	0.14	0.04	0.06	0.04
Na ₂ O	1.89	0.16	1.66	0.15	1.79	0.06	1.70	0.04	1.58	0.06	1.73	0.06	1.70	0.04	1.67	0.14	1.72	0.10	1.71	0.28	1.76	0.10
MgO	7.47	0.51	7.82	0.42	6.44	0.23	7.42	0.24	7.06	0.20	7.42	0.43	7.30	0.24	7.30	0.23	7.48	0.10	6.38	0.19	6.37	0.17
FeO	5.91	0.64	5.27	1.01	5.50	0.27	5.88	0.11	5.71	0.45	5.88	0.11	5.71	0.43	5.47	0.26	5.62	0.22	5.64	0.22	5.69	0.33
MnO	0.02	0.03	0.02	0.02	0.01	0.02	0.02	0.01	0.02	0.02	0.10	0.02	0.08	0.06	0.09	0.06	0.16	0.06	0.02	0.02	0.02	0.02
F	0.20	0.13	0.06	0.07	0.07	0.07	0.07	0.07	0.07	0.07	0.07	0.07	0.07	0.07	0.07	0.07	0.07	0.07	0.07	0.07	0.07	0.07
Total	85.87	0.65	86.10	0.96	80.82	2.25	86.36	0.67	86.20	0.68	86.48	0.38	86.36	0.67	86.14	1.44	85.94	1.10	82.13	0.98	81.69	0.04
Si (T-site)	6.01	0.03	5.95	0.07	5.95	0.06	5.97	0.03	5.97	0.04	5.94	0.04	5.97	0.03	5.98	0.05	5.93	0.08	5.98	0.04	5.93	0.04
Al (T-site)	0.01	0.01	0.06	0.05	0.05	0.05	0.06	0.04	0.03	0.03	0.06	0.04	0.04	0.03	0.03	0.03	0.07	0.08	0.03	0.03	0.07	0.04
Al (Z-site)	6.00	0.00	6.00	0.00	6.00	0.00	6.00	0.00	6.00	0.00	6.00	0.00	6.00	0.00	6.00	0.00	6.00	0.00	6.00	0.00	6.00	0.00
Al (Y-site)	0.28	0.11	0.28	0.09	0.40	0.06	0.29	0.14	0.34	0.03	0.29	0.14	0.34	0.04	0.43	0.05	0.34	0.11	0.44	0.08	0.44	0.08
Cr (Y-site)	0.01	0.00	0.01	0.00	0.01	0.00	0.02	0.01	0.03	0.03	0.02	0.01	0.03	0.03	0.00	0.00	0.00	0.00	0.02	0.01	0.01	0.01
Mg	1.82	0.13	1.90	0.10	1.68	0.03	1.81	0.11	1.77	0.06	1.81	0.11	1.77	0.06	1.77	0.05	1.82	0.05	1.64	0.05	1.65	0.05
Fe	0.81	0.09	0.72	0.13	0.81	0.05	0.80	0.06	0.80	0.06	0.80	0.06	0.78	0.06	0.74	0.03	0.77	0.04	0.81	0.03	0.83	0.05
Mn	0.00	0.00	0.00	0.00	0.00	0.00	0.00	0.00	0.00	0.00	0.00	0.00	0.00	0.00	0.00	0.00	0.00	0.00	0.00	0.00	0.00	0.00
Ti	0.07	0.02	0.08	0.02	0.10	0.01	0.08	0.04	0.07	0.01	0.08	0.04	0.07	0.01	0.04	0.02	0.07	0.04	0.08	0.02	0.07	0.03
Ca	0.09	0.03	0.18	0.03	0.21	0.02	0.18	0.07	0.16	0.02	0.18	0.07	0.16	0.02	0.11	0.04	0.15	0.04	0.17	0.05	0.17	0.05
Na	0.60	0.05	0.52	0.04	0.61	0.02	0.55	0.02	0.54	0.01	0.55	0.02	0.54	0.01	0.53	0.04	0.55	0.03	0.57	0.09	0.59	0.04
K	0.00	0.00	0.00	0.00	0.00	0.00	0.00	0.00	0.00	0.00	0.00	0.00	0.00	0.00	0.00	0.00	0.00	0.00	0.00	0.00	0.00	0.00
Vacancy (Σ□)	0.30	0.07	0.30	0.03	0.17	0.04	0.27	0.09	0.30	0.03	0.27	0.09	0.30	0.03	0.36	0.06	0.30	0.06	0.25	0.12	0.23	0.08

Values in weight percent with total Fe as FeO. Atoms per formula unit based on T + Z + Y = 15 cations (Henry et al. 2011)

tourmaline. The reference materials were analyzed at the start and end of each daily session and before changing samples. Internal precision of each analysis was typically $\pm 0.5\%$ (1 SD). The repeatability from multiple analyses of the schorl and dravite individually (1 SD/mean) was 0.8 and 1.3%, respectively, and 1.7% taken together. The latter value is an estimate of the overall uncertainty as it includes whatever chemical matrix effect is present. We also used the average IMF value from schorl and dravite analyses combined to correct the measured $^{11}\text{B}/^{10}\text{B}$ ratios of the unknowns. During one of the two analytical sessions, there was a systematic linear drift in IMF values, which we ascribe to aging of the electron multiplier (see also Garda et al., 2009b). In this case, the IMF correction was calculated for each analysis individually based on its position in the sequence and a linear regression of reference tourmaline values measured over the entire session. Least-squares regression of 50 reference analyses (combining 25 schorl and 25 dravite results) yielded an R^2 value of 0.959 (standard error 0.3%). Repeatability for this session, calculated from the reference analyses after drift correction, is 1.2% (1 SD /mean). After IMF correction, the $^{11}\text{B}/^{10}\text{B}$ ratios are expressed in the standard delta notation relative to NIST SRM-951, using the value of $^{11}\text{B}/^{10}\text{B} = 4.04362$ from Catanzaro et al. (1970), thus $\delta^{11}\text{B} = [(^{11}\text{B} / ^{10}\text{B})_{\text{sample}} / (^{11}\text{B} / ^{10}\text{B})_{\text{SRM-951}} - 1] \times 1000$.

For the LA-ICP-MS analyses, 80- μm -thick polished sections of samples MP-08b and MP-18 were prepared from the same sample billets as the thin sections used for microprobe and SIMS. Analyses were performed using a New Wave UP-213 laser ablation system coupled to an Elan 6100DRC ICP-MS instrument at the Chemistry and ICP Laboratory, part of the *Núcleo de Apoio à Pesquisa Geoanalítica*, at the Geosciences Institute of the University of São Paulo (USP, Brazil). The procedures are described in Andrade et al. (2014). Briefly, the analytical conditions for spot mode were a laser frequency of 10 Hz, 85% power, and laser fluence of 8.39 J/cm², which resulted in crater diameters of 40 to 65 μm . Some analyses were performed on rastered lines (indicated by the suffix “line” in Table 2), for which the ablated lines were 100 to 120 μm long and 30 to 40 μm wide, with the beam moving at 2 $\mu\text{m}/\text{s}$, a laser frequency of 10 Hz, 70% power, and laser fluence of 1.92 J/cm². The average analysis time was 120 s including 60 s for the blank with the laser off. Reference materials used for calibration were synthetic glasses BHVO-2G, BCR-2G (USGS), and SRM-612 (NIST). Data were reduced during each analysis by means of the Glitter 4.4.2 software (www.glitter-gemoc.com) for instrumental drift and fractionation corrections, adopting NIST SRM-612 as the internal standard. The results listed in Table 2 were adjusted using the known MgO contents determined by electron microprobe (Garda et al. 2009a). We applied detection limit filtering using the Glitter

software and only list data in Table 2 that are above detection limits.

Results

Major and minor elements

All tourmaline from the PM deposit, regardless of type, has compositions corresponding to the alkali group in the classification of Henry et al. (2011), with X-site vacancies from about 20 to 45 atomic % (Fig. 5a). In the Al-Mg-Fe plot of Henry and Guidotti (1985), the samples cluster in fields 4 and 5 on the Al-rich side of the schorl-dravite join (Fig. 5b). As noted by previous studies, the tourmaline at PM is dravitic, with a total range of Mg/(Mg+Fe) between 0.59 and 0.83, clustering around the mean value of 0.69 (1 SD = 0.03). Total Al values are in the range of 6.2 to 6.6 atoms per formula unit (apfu). The positive correlation of Al in the Y-site (0.2 to 0.6 apfu) with vacancies in the X-site ($R^2 = 0.7$) on the one hand, and with Mg on the other ($R^2 = 0.7$), suggests that “excess” Al is charge-balanced by the exchange vector $\text{NaMg}(\text{Al}\square)_{-1}$. Important is the contrast between the Al-rich nature of PM tourmaline and the Al-poor nature of tourmaline from hematite-bearing deposits farther north in the Quadrilátero Ferrífero and Serra do Espinhaço, which have less than 6 apfu Al (balanced by Fe^{3+}) and trend toward the povondraite end member on a plot like Fig. 5b. Cabral et al. (2012a, b) took the unusual composition of tourmaline in those examples, along with other features, to argue for an evaporitic source of the boron (see “Discussion”). Ferric iron was not measured in our study, but there is no Fe-Al correlation in the data to suggest that it is an important component, and the graphite-bearing host rocks preclude high redox conditions (graphite is included in tourmaline). Oliveira et al. (2002) included three samples from Passagem de Mariana in a Mössbauer spectroscopy study and reported between 0 and 12% ferric iron. The minor constituents Ca and Ti share a similar range of concentration, about 0.2 to 1.2 oxide wt% and they are positively correlated with each other ($R^2 = 0.7$). Chromium oxide contents range from below detection limit of 0.01 wt% up to an exceptional value of 0.5 wt%; most analyses fall below 0.2 wt% (see Table 2 for Cr contents by LA-ICP-MS). Fluorine was measured by Garda et al. (2009a), who reported concentrations of 0.01 to 0.25 wt% F. The tourmaline associations T1, T2, and T3 overlap completely in terms of major-element features described above (Fig. 5a, b). Whereas T1 grains are unzoned, the larger, color-zoned grains of types T2 and T3 show a consistent increase in TiO_2 and CaO contents from cores to rims, corresponding to the color change from pale green-tan to dark olive-brown.

Table 2 Trace-element concentrations of tourmaline by laser ablation ICP-MS (values in ppm)

Sample Texture Spot ^a	MP88 Matrix 1a	MP88 Matrix 1b	MP88 Matrix 1c	MP88 Matrix 4a	MP88 Matrix 4b	MP88 Matrix 5L	MP88 Matrix 11L	MP18 Matrix 15L	MP18 Matrix 21	MP18 Matrix 22	MP18 Matrix 23	MP18 Matrix 24
P	34.6	27.5	31.2	45.8	25.3	81.4	87.9	18.1	21.4	38.7	30.5	33.7
Ti	3776	3896	6593	1438	3416	2457	5454	2877	4555	4495	4435	5094
Cr	1205	1377	1590	625	974	839	377	27	106	115	60	179
Rb	0.03	0.03	0.67		0.03		0.12			0.08	0.08	0.08
Sr	143	159	238	86	152	108	217	99	192	179	166	221
Y	0.11	0.19		0.03	0.10			0.01	0.10	0.10	0.07	0.21
Zr	16.7	16.5	0.1		14.0	0.3	0.8	0.4	2.3	6.3	2.3	13.5
Nb	0.06	0.07	0.07		1.25	0.09	0.11	0.05	3.89	1.26	0.23	5.81
Ba	0.21	0.27	4.46	2.80	0.12		0.86	0.91	0.56	1.64	0.47	0.44
Hf	0.39	0.37			0.32		0.12		0.16	0.34	0.11	0.44
Ta	0.01	0.01	0.02		0.04		0.04	0.03	0.36	0.09	0.03	0.63
Pb	14.5	12.9	7.6	8.1	13.0	11.5	10.0	4.0	15.9	15.3	13.3	24.4
Th	0.011	0.044			0.019		0.075	0.015	0.075	0.980	0.254	0.215
U	0.15	0.27			0.11	0.01		0.00	0.05	0.08	0.05	0.20
Co	2.50	2.21	1.01	2.93	1.34	2.79	1.04	0.08	0.95	0.55	0.48	1.11
Ni	14.2	15.7	49.2	12.3	16.2	15.5	36.9	9.3	18.0	18.8	14.9	23.9
Cu	0.44	0.174	0.74		0.16	0.61	0.95	0.68	0.62	0.62	0.44	0.49
Zn	115	101	67.7	102	72.4	104	89.9	56.3	109	99.4	86.2	140.8
Sc	13.6	14.2	33.5	17.3	13.1	15.6	39.0	8.7	14.0	14.0	15.3	10.6
V	155	141	296	95	125	119	274	140	204	207	201	158
La	0.047	0.079	0.781	0.048	0.077	0.030	0.640	0.199	0.179	0.186	0.119	0.301
Ce	0.100	0.119	1.350		0.110	0.054	1.090	0.386	0.298	0.374	0.271	0.428
Pr	0.011	0.010	0.099		0.006		0.076	0.035	0.050	0.029	0.022	0.040
Nd	0.053		0.430		0.033		0.330	0.080	0.112	0.088	0.075	0.162
Sm		0.016					0.087	0.015	0.041		0.028	
Eu	0.072	0.069	0.500	0.055	0.080	0.040	0.540	0.153	0.189	0.231	0.083	0.150
Gd		0.043						0.02		0.065	0.021	
Tb		0.0104								0.0039	0.0025	
Dy	0.027	0.033		0.075				0.013		0.027	0.031	
Ho	0.011	0.011										0.012
Er	0.015	0.029		0.039	0.009						0.007	0.032
Tm					0.005	0.003						
Yb	0.031	0.096		0.141	0.032				0.035	0.084	0.037	0.061
Lu	0.008	0.014							0.002		0.006	0.012

Sample Texture Spot ^a	MP18 Comb 2	MP18 Comb 3	MP18 comb 3a	MP18 Comb 3b	MP18 Comb 4	MP18 Comb 5	MP18 Comb 5L	MP18 Comb 6	MP18 Comb 7L	MP18 Comb 11
P	30.0	28.1	28.3	34.0	22.6	32.5	17.8	22.9	14.7	26.0
Ti	1199	3896	1918	3236	1498	4135	4016	1858	4855	2877
Cr	3.77	7.38	5.32	6.98	3.94	7.11	8.16	7.38	25.7	104
Rb				0.04						0.41
Sr	56.7	137	75.6	112	60.9	115	98.8	72.5	108	94.5
Y	0.00	0.04								0.04
Zr		0.21	0.14	0.20	0.19	0.01		0.17	0.17	1.54
Nb	0.01	0.04	0.03	0.05	0.04	0.07	0.02	0.03	0.02	0.10
Ba		0.60	0.20	0.28	0.06	0.53	0.16	0.10	0.19	5.69
Hf						0.03			0.02	0.05
Ta	0.00	0.01		0.00					0.01	0.01
Pb	3.62	6.4	4.66	6.92	4.58	7.31	9.18	3.75	7.41	7.54
Th		0.021			0.009	0.009				0.085
U			0.00			0.00				0.12
Co	0.07	0.10	0.06	0.07	0.12	0.07	0.10	0.07	0.07	1.69
Ni	9.26	10.24	9.56	8.61	10.02	9.20	9.63	9.35	8.55	13.8
Cu	0.21	0.66		0.41		0.22	0.75	0.15	0.57	0.357
Zn	59.2	69.6	74.0	59.0	67.2	64.7	60.7	62.3	63.1	90.6
Sc	6.68	14.1	12.2	10.7	11.6	12.8	12.0	10.5	11.6	16.8
V	121	237	151	228	111	222	231	159	311	150
La	0.020	0.121	0.046	0.059	0.026	0.050	0.039	0.037	0.039	0.109
Ce	0.038	0.241	0.068	0.109	0.059	0.083	0.092	0.056	0.134	0.183
Pr	0.003	0.017	0.006	0.009			0.009	0.005	0.012	0.018

Table 2 (continued)

Nd	0.026	0.069					0.038			0.113
Sm				0.016						
Eu	0.022	0.089	0.035	0.050	0.022	0.044	0.042	0.025	0.041	0.106
Gd	0.024									0.019
Tb		0.003	0.003						0.002	0.003
Dy			0.006							0.018
Ho		0.003						0.002		
Er						0.012				0.011
Tm										
Yb										
Lu				0.003						

All samples are type T2 tourmalines

^a Spot analyses except where indicated by L (line scan)

Trace-element variations

In situ analysis by laser ablation ICP-MS could not be made for the T1 tourmaline because of its small grain size (typically below 20 μm) and the presence of mineral inclusions. The samples investigated in this study (MP8B and MP18) are therefore limited to tourmaline association T2, including both matrix-hosted grains and those with comb texture that grew into the margin of a quartz vein (Table 2). Cabral and Koglin (2012) published LA-ICP-MS analyses of tourmaline of type 3 intergrown with arsenopyrite in a sample from the quartz lode at the Fundão orebody, level 315. This is the same locality as our sample MP18 from the wall-rock alteration zone (type T2), so the two samples can be directly compared. The results of our analyses together with data from Cabral and Koglin (2012) are shown on a multi-element plot normalized to average continental crust (Fig. 6a) and a chondrite-normalized REE plot (Fig. 6b) along with whole-rock data from two samples of the Batatal phyllite from Spier (2007) for comparison. The plots illustrate three main features of the PM tourmaline: low abundances of trace elements overall, large variations within samples, and little correspondence in trace-element patterns between tourmaline and bulk rock. The Batatal phyllite is similar to the average upper crust in Fig. 6a (except for low Sr, Zn), but in tourmaline, only a few elements reach concentration levels at or above those of the average crust (Zn, Pb, Cr, Ga, V, Sc, and Ti). The chondrite-normalized REE plot (Fig. 6b) also shows overall low concentrations and a high variability of the PM tourmaline. The Batatal phyllite has 220–230 ppm total REE, compared with a maximum total REE of 7.4 ppm in T3 tourmaline (an outlier value). Overall, the T3 data from Cabral and Koglin (2012) show higher REE values than T2 but with considerable overlap and a large variation in all samples. The T3 total REE contents range from 0.3 to 7.4 ppm, T2 in sample MP8B has total REE from 0.13 to 3.2 ppm, and in sample MP18 the tourmaline yielded 0.11 to 1.2 ppm total REE. Despite the low and variable ranges of concentration,

most tourmaline from the PM deposit shows a similar pattern on Fig. 6b, with a consistent rise from the middle to light REE concentrations (normalized La/Nd ratio near 3), a flat but poorly defined middle to heavy REE segment, and a strong positive Eu anomaly. Apart from the Eu anomaly, the tourmaline REE patterns are not dissimilar to those of the host Batatal phyllite.

Element correlations and discrimination features are examined in plots of selected trace elements with Ti in Fig. 7. Strong positive correlations exist between Ti and Sr and Pb and V. Titanium also correlates positively with Cr in T2 sample MP8B and in the T3 data, but a second sample of T2, MP18, has very low Cr values with no relation to Ti (Fig. 7d). Not all elements analyzed in this study were included in the study of Cabral and Koglin (2012), but comparisons are possible for Cr (Fig. 7d), Co, and Ni (see Fig. 8 and discussion of Co/Ni ratio below) and for the chalcophile elements Cu and Zn (Fig. 7e, f). For both of the latter and particularly for Zn, the vein-hosted T3 tourmaline has higher concentrations than tourmaline from wall-rock alteration zones. This we attribute to the closer relationship of T3 tourmaline to ore mineralization, whereas T2 compositions are partly controlled by the wall rock. Although arsenopyrite is the dominant ore mineral in the Passagem deposit, Cu and Zn minerals are also present in minor amounts, namely chalcopyrite, sphalerite, and tennantite (Chauvet et al. 2001, Vial et al. 2007).

Boron-isotope compositions

The full range of $\delta^{11}\text{B}$ values determined in tourmaline from the PM deposit is -17.8 to -7.1‰ ($n = 49$), listed in Table 3. Correlations between the B-isotope ratio of spot analyses and the corresponding major-element compositions were tested for and not found. In grains sufficiently large and free of inclusions for multiple analyses, we also found no within-grain variations larger than analytical uncertainty, even for the color-zoned T2 tourmaline in sample MP8B (Fig. 4d). In fact, nearly all samples analyzed are isotopically

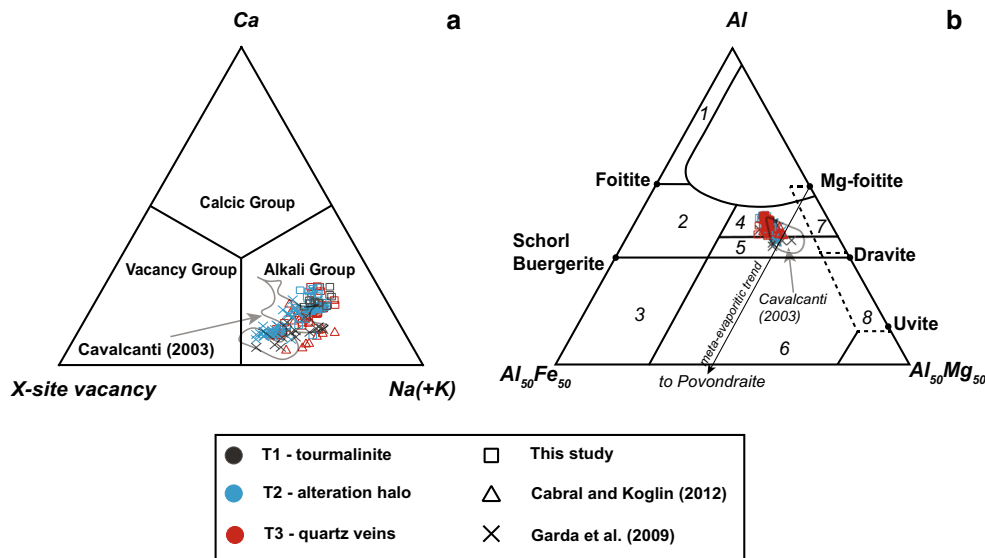


Fig. 5 Ternary classification plots of Passagem de Mariana tourmaline in terms of **a** Ca-X-site vacancy-Na+K (after Hawthorne and Henry 1999) and **b** Al-Fe-Mg contents (after Henry and Guidotti 1985). The fields on **b** denote typical tourmaline compositions from: (1) Li-rich granitoid, pegmatites, aplites; (2) Li-poor granitoids, pegmatites, aplites; (3) Fe³⁺-rich quartz-tourmaline rocks; (4) metapelites and metapsammites with an Al-saturating phase; (5) metapelites and metapsammites without an Al-saturating phase; (6) Fe³⁺-rich quartz-tourmaline rocks, calc-silicate

rocks, and metapelites; (7) low-Ca meta-ultramafics and Cr, V-rich metasediments; and (8) metacarbonates and meta-pyroxenites. The PM tourmalines define a relatively narrow cluster corresponding to the alkali group with Al-rich, dravite-schorl compositions. The arrow toward povondraite (end-member NaFe³⁺₃Fe³⁺₆(BO₃)₃Si₆O₁₈(O, OH)₄) illustrates a trend found in tourmaline from other auriferous deposits in the Quadrilátero Ferrífero (Cabral et al. 2012a, b) and attributed to meta-evaporite protoliths

homogeneous within the uncertainty of 1.5‰ (1 SD). An overview of the results for the three tourmaline types is shown as a histogram in Fig. 9, and in detail, the statistical summary of the B-isotope results for the six samples is as follows:

- T1 (tourmalinite) MP1 = -14.5 ± 1.5‰, n = 11; PM16 = -12.0 ± 1.2‰, n = 4
- T2 (alteration halo) MP8B = -14.1 ± 1.7‰, n = 9; MP18 = -14.3 ± 0.8‰, n = 7; PM38A = -12.9 ± 2.0‰, n = 8; PM33B = -14.5‰, n = 2
- T3 (quartz veins) PM38B = -8.9 ± 1.3‰, n = 8

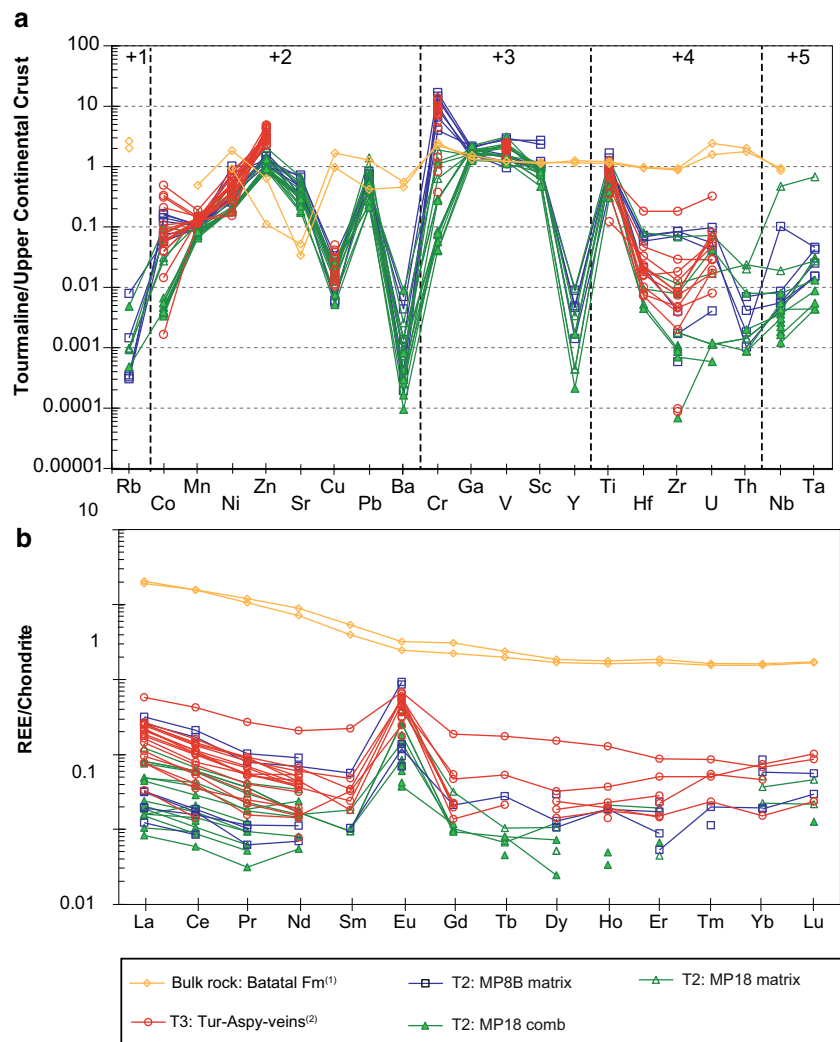
There is no significant difference in the B-isotope range of tourmalinite grains (T1) and those from the wall-rock alteration (T2). Taking all T1 and T2 analyses together (Fig. 9) yields indistinguishable mean values of -13.9 ± 1.9 and -13.8 ± 1.6‰, respectively. In contrast, vein-hosted T3 tourmaline has significantly higher values of -11.5 to -7.1‰ with a mean of -8.9 ± 1.3‰. The contrast between T2 and T3 tourmaline is also seen at the thin-section scale. Sample PM38 straddles the contact between the quartz vein and selvage. The tourmaline from the selvage (PM38A) and the vein (PM38B) yielded δ¹¹B averages more than 5‰ apart (-14.5 and -8.9‰, respectively).

Discussion

The relationship of stratiform tourmalinite to mineralization

The literature contains conflicting views on the origin of stratiform tourmalinites in the host rocks of Passagem de Mariana deposit. These were considered as be syn-sedimentary by Fleischer and Routhier (1973) and again by Cavalcanti and Xavier (2006). However, Vial et al. (2007) argued for a hydrothermal origin related to quartz veining. This was based on the presence of S1-fabric orientation of mineral inclusions within the tourmaline grains (locally refolded by S2), indicating post-sedimentary growth, and on underground mapping that showed that tourmalinite lenses occur in all lithologies at the PM deposit, but only in the vicinity of quartz veins, and that the tourmaline abundance increases toward the veins. Our study adds compositional observations to the debate on tourmalinite origin. We have shown (Fig. 5) that the T1 and T2 tourmalines have the same dravitic, Al-rich chemical compositions with complete overlap in terms of minor element variations such as Ca and Ti. In addition to the chemical similarity, we documented a complete correspondence in the B-isotope range and mean values for the T1 and T2 associations (Fig. 9). Thus, the compositional evidence is in favor of the hypothesis that PM tourmalinites formed, or at least were thoroughly overprinted

Fig. 6 Display of trace-element variations in Passagem de Mariana tourmalines and in the phyllite host rocks normalized to **a** upper continental crust (from Rudnick and Gao 2014, ordered by valence and radius after Klemme et al. 2011) and **b** chondrite (from Taylor and McLennan 1985). Data for T3 tourmaline (Tur-Aspy veins)² are from Cabral and Koglin (2012). Data for Batatal Formation phyllite (Batatal Fm)¹ are from Spier (2007)



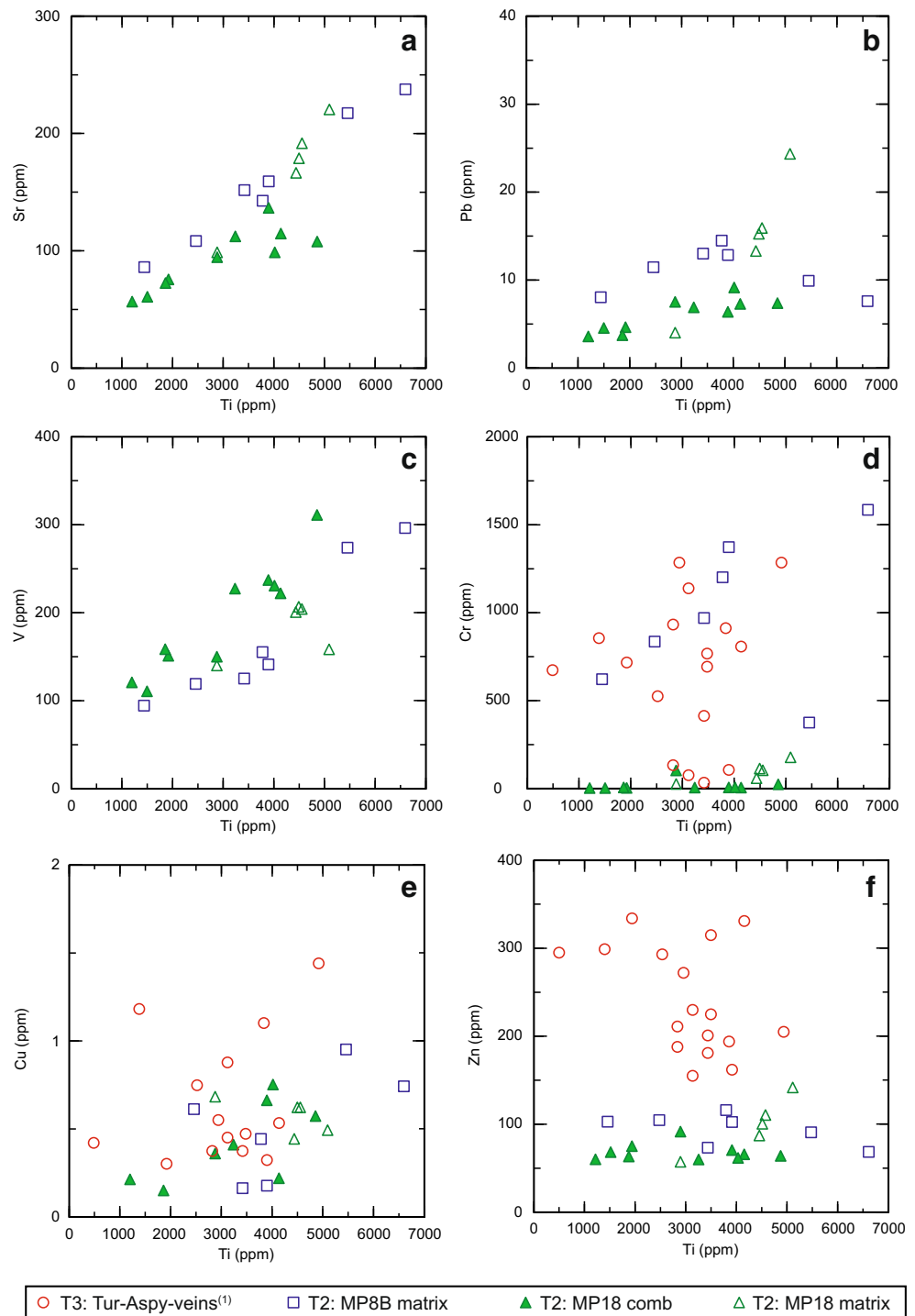
by, boron metasomatism related to the hydrothermal mineralization. Less clear is the relative timing of tourmaline formation with respect to metamorphism and deformation in the host rocks. Vial et al. (2007) placed tourmaline formation late in D2, which they equate to the Transamazonian orogeny at around 2.1 Ga. They dismissed the mica ^{40}Ar - ^{39}Ar ages of 485 to 490 Ma reported by Chauvet et al. (2001) as thermal resetting in the “Brasiliano” orogeny. However, a U-Pb age of 496 ± 2 Ma from hydrothermal xenotime in a tourmaline-rich vein “pocket” in the PM deposit indicates at least some of the tourmaline formed at that time (Cabral and Zeh 2015).

Trace elements in tourmaline and the Co/Ni index

First-order features of trace element contents in tourmaline from this study are the low to very low abundances of a large number of elements including the REE, a high variability of element concentrations in single samples, and a pronounced positive Eu anomaly on chondrite-normalized

plots (Fig. 6). The plots in Fig. 6 show that trace-element patterns in PM tourmaline differ from those of the host rock (Batatal formation phyllite from Spier 2007), which for example has a moderate negative Eu anomaly and total REE concentrations of about 220 ppm (typically 1–3 ppm in tourmaline). Similar features have been noted in other LA-ICP-MS studies of tourmaline from diverse settings including granites and related veins (Marks et al. 2013, Duchoslav et al. 2017, Yang et al. 2015, Hazarika et al. 2017) and clastic metasedimentary and metavolcanic rocks (van Hinsberg and Schumacher 2011, Redler et al. 2016, Berryman et al. 2017, Adlakha et al. 2017, Kalliomäki et al. 2017). In particular, a positive Eu anomaly appears to be characteristic, having been found in most of the studies cited above, regardless of the host rock and the magmatic, hydrothermal or metamorphic origin. This means that a positive Eu anomaly in tourmaline, as in plagioclase, does not indicate unusual redox conditions. Also common for tourmaline from many settings is a concave-upward REE

Fig. 7 Variation diagrams of selected trace element contents versus Ti (in ppm) in tourmaline from the Passagem de Mariana gold deposit. Data for T3 tourmaline (Tur-Aspy veins)¹ are from Cabral and Koglin (2012)



pattern, suggesting a relative preference of light and heavy REE over middle REE in the structure. In the PM tourmaline (Fig. 6b), the middle and heavy REE concentrations are in many cases near or below detection limit so the REE patterns are poorly defined. Indeed, the low and variable trace-element contents of tourmaline are currently a limitation to the use of this mineral as a source proxy or vector

to mineralization, and much remains to be learned about the systematics of trace-element partitioning in tourmaline (see van Hinsberg 2011). Nevertheless, our study showed higher Cu and Zn contents in vein-hosted tourmaline relative to wall rocks and Duchoslav et al. (2017) reported that tourmaline from Cornish tin lodes has high Sn values compared with tourmaline in related granite.

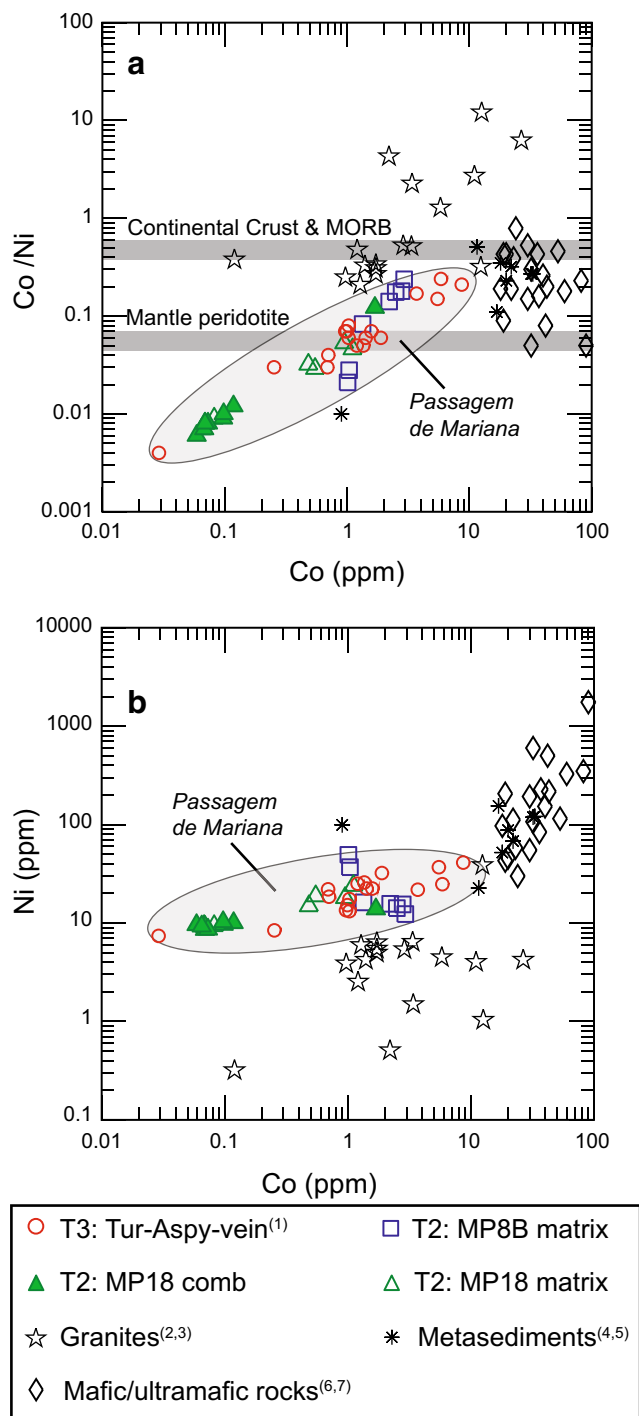


Fig. 8 Display of Co vs the Co/Ni ratio (a) and Co vs Ni contents (b) in tourmaline from Passagem de Mariana (this study and Cabral and Koglin 2012, shaded field) compared with tourmaline data from mafic-ultramafic rocks (6,7: Galbraith et al. 2009, Baksheev et al. 2017), granites and pegmatites (2,3: Marks et al. 2013, Hazarika et al. 2017, Yang et al. 2015), and metasedimentary rocks (4,5 van Hinsberg and Schumacher 2011; Kalliomäki et al. 2017). The Co/Ni ratios of average continental crust, MORB, and peridotite mantle in plot (a) are from Rudnick and Gao (2014) and Hofmann (1988). See text for discussion

Cabral and Koglin (2012) used the Co/Ni ratio in vein tourmaline (T3) and arsenopyrite from Passagem de

Table 3 Boron isotope ratios of tourmaline by SIMS

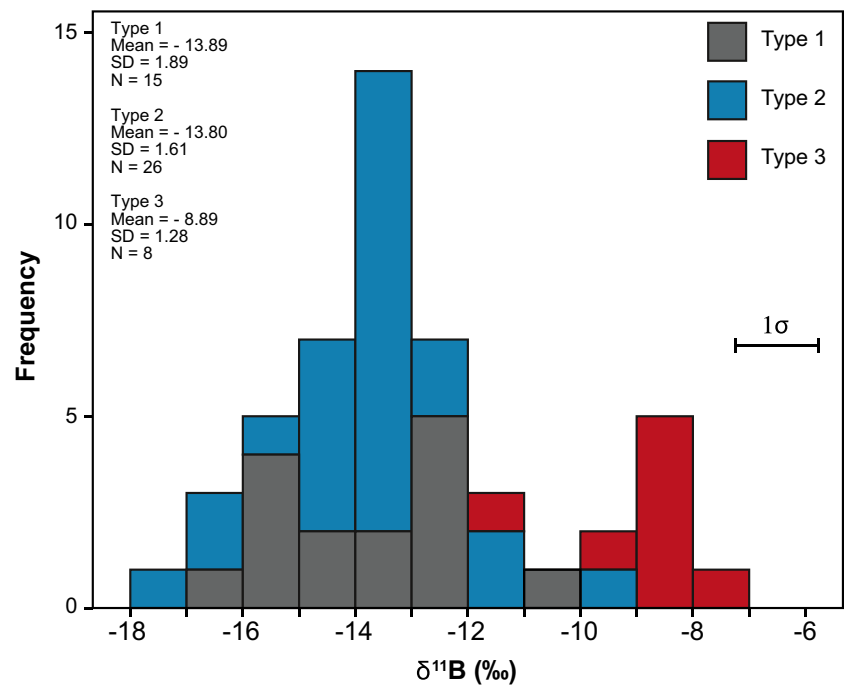
Type	Sample	$\delta^{11}\text{B}$ (‰)	Type	Sample	$\delta^{11}\text{B}$ (‰)	
T1	PM16	-13.0	T2	MP8B	-12.2	
	PM16	-12.2		MP8B	-17.8	
	PM16	-10.2		MP8B	-15.7	
	PM16	-12.5		MP8B	-13.8	
	MP1	-17.0		MP8B	-13.2	
	MP1	-14.9		MP8B	-13.4	
	MP1	-12.7		MP8B	-13.3	
	MP1	-12.4		MP8B	-13.8	
	MP1	-13.1		MP8B	-13.2	
	MP1	-15.4		MP18	-13.9	
	MP1	-14.8		MP18	-13.6	
	MP1	-13.7		MP18	-13.8	
	MP1	-15.4		MP18	-14.2	
	MP1	-15.4		MP18	-14.4	
	MP1	-15.6		MP18	-16.1	
T2	PM38A	-14.0	T3	PM38B	-9.7	
	PM38A	-14.5		PM38B	-8.6	
	PM38A	-13.3		PM38B	-8.6	
	PM38A	-11.5		PM38B	-8.1	
	PM38A	-12.2		PM38B	-11.5	
	PM38A	-12.0		PM38B	-8.6	
	PM38A	-9.7		PM38B	-7.1	
	PM38A	-16.1		PM38B	-8.9	
	PM33B	-14.0				
	PM33B	-15.0				

Analytical uncertainty is estimated at 1.7‰ (1 SD, see text)

$^{11}\text{B}/^{10}\text{B}$ expressed as $\delta^{11}\text{B}$ values relative to NIST SRM-951

Mariana to argue for a crustal source of the metals and suggested that this may be a useful source index in general. They derived an average Co/Ni ratio of about 0.5, close to the upper-crustal value of 0.37 (Rudnick and Gao 2014). While we agree that a crustal source of Co, Ni, and other metals is reasonable for the PM deposit, it is noted that the Co/Ni ratio in global mid-ocean ridge basalts (MORB) is about the same as the crust (0.47 after Gale et al. 2013), so those two reservoirs are not discriminated. However, mantle peridotite does have a distinct and low Co/Ni ratio because of the high abundance of Ni in olivine (mantle Co/Ni = 0.05: Hofmann 1988). Our LA-ICP-MS results for T2 tourmaline (Table 2 and Fig. 8) yielded Co/Ni ratios not far from the mantle value (i.e., 0.03 ± 0.03 in MP18 and 0.11 ± 0.09 in MP8B), which at first glance might suggest an ultramafic source lithology. That is inconsistent with the value of 0.5 from Cabral and Koglin (2012), but the very low and variable concentrations in tourmaline, particularly for Co, urge caution in

Fig. 9 Frequency histogram and statistical summary of B-isotope ratios of tourmaline types 1, 2, and 3 from Passagem de Mariana



this comparison (Fig. 8). The Co/Ni ratio of arsenopyrite is 0.14–0.89, average 0.47 (Cabral and Koglin 2012), and this seems a more reliable ratio because the Co and Ni concentrations are in the hundreds of parts per million. Since Cabral and Koglin (2012), many LA-ICP-MS studies provide Co and Ni data that can be used to further test the use of Co/Ni as a source index. Figure 8 shows a compilation from various settings including mafic and ultramafic schists hosting emerald mineralization, clastic metasedimentary rocks, and crustal granites and pegmatites (see figure caption for references). We observe that tourmaline from mafic and ultramafic schists (talc schists, serpentinites, chlorite schists) has Co/Ni ratios between that of MORB and the mantle value. Furthermore, those tourmalines have high Ni and Co concentrations (Fig. 8b) and the two elements are well correlated, which is not the case for the PM tourmaline shown on the same plots. In these examples, the Co/Ni ratio correctly indicates an ultramafic source. Conversely, the metasedimentary rock-hosted tourmaline and some tourmaline from granites correspond to the Co/Ni value of average crust, but many of the granite-hosted tourmalines have much higher ratios. We attribute the latter to fractional crystallization. Since tourmaline in granites tends to be a late-magmatic phase and Ni is more compatible than Co in mafic silicates and Fe-Ti oxides (www.GERM.org), fractionation will lower the Co/Ni ratio. In summary, the Co/Ni ratio in tourmaline may be useful as a source index in some cases, particularly for detecting an ultramafic source, but it should be applied with discretion.

B-isotope variations in wall rock and vein-hosted tourmaline

The wall-rock tourmaline types T1 (tourmalinite) and T2 (vein selvage) have nearly the same range of $\delta^{11}\text{B}$ values (-17.0 to -10.2‰ and -17.8 to -9.7‰ , respectively) and indistinguishable mean values of -13.9 and -13.8‰ (Table 3 and Fig. 9). In contrast, the vein-hosted T3 tourmaline has consistently higher $\delta^{11}\text{B}$ values (-11.5 to -7.1‰) with a mean of -8.9‰ that is about 5‰ offset from the T1 and T2 average. In principle, this difference could be caused by a temperature change between veins and wall rocks at constant fluid composition, by different boron sources and varying mixing proportions in the vein fluid vs. wall rocks, or by an isotopic shift in the fluid composition caused by preferential ^{10}B uptake by tourmaline during wall-rock tourmalinization (Rayleigh fractionation). Considering the temperature effect alone, the fractionation factors of Meyer et al. (2008) indicate that a shift in $\delta^{11}\text{B}$ by 5‰ requires cooling by about 300 °C . Chauvet et al. (2001) estimated the temperature of mineralization at $350\text{--}400\text{ °C}$ from arsenopyrite thermometry. Further cooling by 300 °C before crystallization of wall-rock tourmaline is unrealistic and we recall that T2 and T3 tourmalines from a single thin section (sample PM38B) show the same 5‰ contrast. Thus, a change in fluid composition and/or boron source seems required. The possibility that different boron sources contributed to vein and wall-rock tourmaline is logical considering that tourmalinization replaces earlier minerals and is strongest in sericite phyllites (Vial et al. 2007). Sheet silicates

are enriched in ^{10}B compared with aqueous fluid, by about 10‰ at 400 °C (Wunder et al. 2005), so tourmaline replacing mica should have a lower $\delta^{11}\text{B}$ value than tourmaline growing in a quartz vein. On the other hand, the amount of boron needed to produce the tourmalinites and tourmaline-rich selvages in the PM deposit cannot be supplied by in-situ replacement of sericite alone, and the fact that tourmaline abundance increases toward vein contacts (Vial et al. 2007) suggests that boron is coming from the vein fluid. Thus, cooling and mica replacement may cause a lowering of $\delta^{11}\text{B}$ in wall-rock tourmaline vs. veins, but the shift is expected to be small. A more realistic explanation is that the formation of abundant tourmaline in wall rocks depleted the hydrothermal fluid in ^{10}B before the crystallization of vein-hosted tourmaline. This implies that the tourmalinization preceded vein mineralization, which agrees with the fact that fragments of tourmalinite are caught up in vein quartz (Fig. 3a). Furthermore, the paragenetic sequence proposed by Chauvet et al. (2001) and Vial et al. (2007) places the onset of tourmaline formation before the sulfide vein mineralization. If this scenario is true, the B-isotope composition of T3 tourmaline reflects a boron-depleted fluid that preferentially lost ^{10}B during wall-rock alteration and is not best suited to constrain the fluid origin. Instead, the relevant value for estimating the original fluid composition is the T1–T2 mean of -14‰ . Using that, and the 350–400 °C mineralization temperature from Chauvet et al. (2001), the fluid composition is predicted to be -11.3 to -10.8‰ .

Implications for fluid sources and gold mineralization in the Quadrilátero Ferrífero

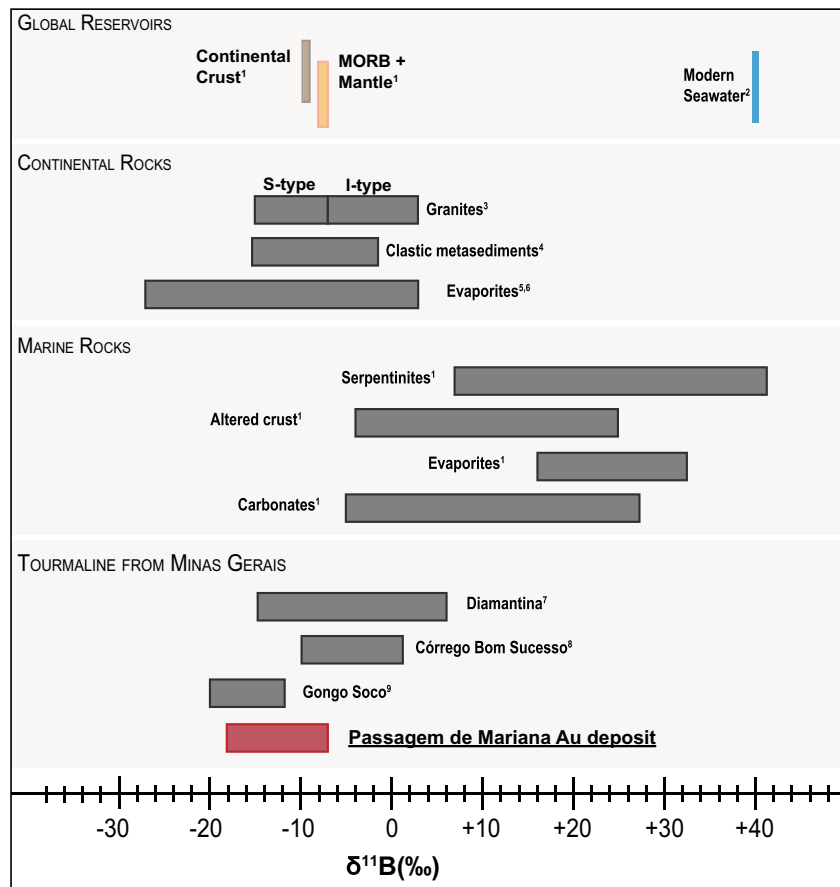
Figure 10 shows a comparison of the $\delta^{11}\text{B}$ values for tourmaline from Passagem de Mariana with those from other hydrothermal deposits of similar age and setting in the Quadrilátero Ferrífero (Gongo Soco) and in the Serra do Espinhaço about 200–250 km further to the north (Córrego Bom Sucesso and Diamantina). Also shown is the compositional range of geologic reservoirs relevant to a discussion of boron sources in these deposits. The first point to make is that tourmalines from the PM and Gongo Soco deposits are similar and isotopically light, whereas the compositions from the Diamantina and Córrego Bom Sucesso range to positive values of $\delta^{11}\text{B}$. The consistently negative $\delta^{11}\text{B}$ values of PM and Gongo Soco tourmaline are clear evidence for a source of boron in the continental crust and against significant contributions from rocks of marine origin or influence (e.g., marine carbonate and evaporite, seafloor-altered basalts, serpentinites). Tourmaline from the Diamantina and Córrego Bom Sucesso deposits has $\delta^{11}\text{B}$ values as high as $+4\text{‰}$ that might suggest a marine influence, especially considering that the fluid will be isotopically heavier than the tourmaline formed from it (see Cabral et al. 2017).

Returning to the negative values of tourmaline from Passagem de Mariana and its estimated fluid composition of -11‰ , the possible sources of boron are granitic magmas, continental metasedimentary rocks, and continental evaporites (Fig. 10). Albert et al. (2018) documented tourmaline with -14‰ from an Archean leucogranite (2716 ± 5 Ma) in the Bação dome northwest of the PM deposit, but we rule out boron from granites because there are no intrusions of appropriate age near the deposit. Cabral et al. (2012a, 2017) argued for a continental evaporite source of boron in the Gongo Soco (and other deposits) based on the distinctive chemical features of tourmaline that indicate oxidizing conditions and a protolith low in aluminum (povondraite substitution: $\text{Fe}^{3+}\text{Al}_{-1}$). That is logical considering the hematite-rich itabirite host rocks and the evaporite model was supported by Lüders et al. (2005) who found high Br/Cl ratios in fluid inclusions suggesting halite dissolution in the source. However, those features would equally fit a marine setting. In fact, Spier (2007), Farina et al. (2016), and Dopico et al. (2017) invoked a marine origin for the Cauê Formation which hosts Gongo Soco, and they do not mention terrestrial evaporites in the Minas Supergroup. The argument for a continental evaporite source based on B-isotopes assumes that the chemical and isotopic compositions of tourmaline are controlled by the same process, which need not be the case. Indeed, the fact that “povondraite” tourmaline from the Gongo Soco deposit and the Al-rich tourmaline hosted by graphitic phyllites at Passagem de Mariana have the same $\delta^{11}\text{B}$ values suggests that chemical and B-isotope compositions are decoupled. Given that the PM deposit is hosted by clastic metasedimentary units of the Batatal and Moeda Formations and that these units are regionally extensive in the Mariana anticline, we consider that metasedimentary rocks are the likely source of the “crustal” B-isotope signature. It should also be stressed that tourmaline is much more abundant at Passagem de Mariana than at Gongo Soco, so the amount of boron in the Itabirite-hosted system is low. Furthermore, it is likely that the metasedimentary package is a better source of ore metals than the chemical sediments of the Cauê Formation (cf. the “crustal” Co/Ni ratio of PM arsenopyrite from Cabral and Koglin 2012).

Conclusions

Three types of tourmaline from the Passagem de Mariana gold deposit have been studied by in situ chemical and B-isotope analyses: fine-grained, stratiform tourmalinite (T1); tourmaline in alteration zones surrounding quartz veins (T2); and tourmaline within quartz veins (T3). Tourmalinite is fine-grained and contains abundant oriented inclusions that parallel fabric in the host rocks. Vein-

Fig. 10 Summary of B-isotope compositions for global boron reservoirs, marine and continental rocks (upper panels), and for tourmaline from gold deposits in Minas Gerais (lower panel). Data sources: 1: Marschall (2018), 2: Palmer and Slack (1989), 3: Trumbull and Slack (2018), 4: Trumbull et al. (2011), 5, 6: Palmer and Slack (1989), Kasemann et al. (2004) 7: Cabral et al. (2012a), 8: Cabral et al. (2011), 9: Cabral et al. (2012b)



selvage and vein-internal T2 and T3 tourmaline grains are larger and commonly zoned, with higher Ti and Ca in rims. All three tourmaline types have Al-rich dravitic compositions with Mg/(Mg+Fe)=0.59 to 0.83 and Al contents of 6.2 to 6.6 apfu. There is no difference in element composition between the stratiform tourmalinite and the other two types, which supports the inference from field observations that all tourmaline is hydrothermal (Vial et al. 2007). The T1 grains are unfortunately too small and inclusion-rich for trace-element analysis by LA-ICP-MS so we can compare only the T2 and T3 tourmaline. The trace-element concentrations in both groups are in general very low compared with the host phyllite, and the distribution patterns do not mirror the host rock, suggesting a crystallographic control. For example, the REE total concentrations in tourmaline are less than 5 ppm compared with 220 ppm for the whole rock, and the chondrite-normalized patterns of tourmaline all display strong positive Eu anomalies, unlike the flat patterns of the bulk rock. The tourmalines from mineralized veins and from wall rocks are similar for most elements, but the T3 tourmaline ranges to higher values for Zn, Cu, and Co, which we attribute to a stronger influence of the ore-forming fluid.

Boron-isotope ratios of tourmaline from both tourmaline associations in the wall rocks (T1 and T2) cover a considerable range in δ¹¹B from -17.8 to -9.7‰, but their mean values are indistinguishable at -13.9 and -13.8‰, respectively. The similarity in B-isotope composition further suggests that the T1 tourmalinite formed by hydrothermal alteration. The vein-hosted tourmaline (T3) has consistently higher δ¹¹B values than tourmaline in the wall rocks (-11.5 to -7.1‰), with a mean of -8.9 ± 1.3‰. None of the tourmaline grains are isotopically zoned or show internal variations beyond the analytical uncertainty of 1.7‰. There is a 5‰ difference between the T2 and T3 tourmaline types, even in a single sample that spans the vein contact. We dismiss the idea that a temperature gradient from vein to wall rocks caused this shift because 300 °C cooling would be required. Mass-balance considerations discount replacement of mica in the host phyllite as an explanation for the low δ¹¹B values in tourmaline T1 and T2. Instead, we suggest that the intensive tourmalinization of the wall rocks progressively depleted the hydrothermal fluid in boron, preferentially in ¹⁰B, leaving fluid in the quartz veins, and the T3 tourmaline that formed from them, with higher δ¹¹B values. This scenario is consistent with the relative abundance of tourmaline in wall rocks and veins and with the paragenetic sequence observed in mine

exposures (Chauvet et al. 2001; Vial et al. 2007). It follows that the isotopic composition of T1 and T2 tourmaline best reflects that of the original hydrothermal fluid. For a temperature of 350–400 °C (Chauvet et al. 2001) and $\delta^{11}\text{B}$ value of -14% for tourmaline, the fluid composition is about -11% . That B-isotope composition is typical for continental metasedimentary rocks and granites, and it is also in the range of continental evaporites. The regional host rocks of the Passagem de Mariana and other gold deposits along the Mariana anticline are clastic metasedimentary units, banded iron formation, and carbonates of the Minas Supergroup. There are no granitic intrusions in the region of appropriate age to act as boron source, and the chemical sediments (carbonates, iron formation) in the Minas Supergroup are shallow marine deposits so evidence of terrestrial evaporites is lacking. Therefore, we conclude that the source of boron in the hydrothermal fluids is likely to be the Batatal and/or Moeda metasedimentary sequences. We support an orogenic gold model for these deposits whereby metamorphic fluids carrying metals and boron from the Minas Supergroup are focused by regional shear zones along the Mariana anticline, possibly related to the Neoproterozoic/Cambrian Brasiliano orogeny. Local differences in the host rocks, especially the redox contrast between graphitic phyllites and the itabirite unit, control the mineralogy of the different deposits (i.e., sulfate/sulfide zonation of Cabral et al. 2013), and the major-element composition of tourmaline within them, but the similarity of B-isotope ratios in the region suggests a common source of the mineralizing fluids.

Acknowledgements G.G. thanks Dr. Sandra Andrade for the in situ LA-ICP-MS analyses performed at the Chemistry and ICP Laboratory of the Geosciences Institute of São Paulo University (Brazil) and FAPESP (Processes 2005/56651-3 and 2007/53895-4) for financial support for the boron isotope study. M.C. is supported by a grant in the BMBF R4 project GRAMME (Germany). The authors are grateful to Shao-Yong Jiang, Alexandre Raphael Cabral, and John Slack for thorough, constructive criticisms of the manuscript that led to major improvements in our interpretation.

References

- Adlakha EE, Hattori K, Davis WJ, Boucher B (2017) Characterizing fluids associated with the McArthur River U deposit, Canada, based on tourmaline trace element and stable (B, H) isotope compositions. *Chem Geol* 466:417–435
- Albert C, Lana C, Gerdes A, Schannor M, Narduzzi F, Queiroga G (2018) Archean magmatic-hydrothermal fluid evolution in the Quadrilátero Ferrífero (SE Brazil) documented by B isotopes (LA MC-ICP-MS) in tourmaline. *Chem Geol* 481:95–109
- Alkmim FF, Marshak S (1998) Transamazonian orogeny in the southern São Francisco craton region, Minas Gerais, Brazil: evidence for Paleoproterozoic collision and collapse in the Quadrilátero Ferrífero. *Precambrian Res* 90:29–58
- Andrade S, Ulbrich HHGJ, Gomes CB, Martins L (2014) Methodology for the determination of trace and minor elements in minerals and fused rock glasses with laser ablation associated with quadrupole inductively coupled plasma mass spectrometry (LA-Q-ICPMS). *Am J Anal Chem* 5:701–721
- Babinski M, Chemale JF, Van Schmus WR (1995) The Pb/Pb age of the Minas Supergroup carbonate rocks, Quadrilátero Ferrífero, Brazil. *Precambrian Res* 72:235–245
- Baksheev IA, Trumbull RB, Popov MP, Erokhin YV, Kudryavtseva OE, Yapaskurt VO, Khiller VV, Vovna GM, Kiselev VI (2017) Chemical and boron isotopic composition of tourmaline from the Mariinsky emerald deposit, Central Urals, Russia. *Min Dep* 53:565–583. <https://doi.org/10.1007/s00126-017-0759-z>
- Baltazar OF, Zucchetti M (2007) Lithofacies associations and structural evolution of the Archean Rio das Velhas greenstone belt, Quadrilátero Ferrífero, Brazil: a review of the setting of gold deposits. *Ore Geol Rev* 32:471–499
- Barbosa ALM, Grossi-Sad JH, Dorr JVN (1974) The “consanguineous” origin of a tourmaline-bearing gold deposit: Passagem de Mariana (Brazil)—discussion. *Econ Geol* 69:416–419
- Berryman E, Kutzschbach M, Trumbull RB, Meixner A, van Hinsberg V, Franz G (2017) Tourmaline as a petrogenetic indicator in the Pfisch Formation, western Tauern window, eastern Alps. *Lithos* 284–285: 138–155
- Cabral AR, Lehmann B, Tupinamba M, Schlosser S, Kwitko-Ribeiro R, de Abreu FR (2010) The platiniferous Au-Pd belt of Minas Gerais, Brazil, and Genesis of its botryoidal Pt-Pd Aggregates. *Econ Geol* 104 (8):1265–1276
- Cabral AR, Koglin N (2012) Hydrothermal fluid source constrained by Co/Ni ratios in coexisting arsenopyrite and tourmaline: the auriferous lode of Passagem, Quadrilátero Ferrífero of Minas Gerais, Brazil. *Mineral Petrol* 104:147–145
- Cabral AR, Zeh A (2015) Detrital zircon without detritus: a result of 496-Ma-old fluid-rock interaction during the gold-lode formation of Passagem, Minas Gerais, Brazil. *Lithos* 212–215:415–427
- Cabral AR, Lehmann B, Tupinambá M, Wiedenbeck M, Brauns M (2011) Geology, mineral chemistry and tourmaline B isotopes of the Córrego Bom Sucesso area, southern Serra do Espinhaço, Minas Gerais, Brazil: implications for Au–Pd–Pt exploration in quartzitic terrain. *J Geochem Explor* 110:260–277
- Cabral AR, Wiedenbeck M, Koglin N, Lehmann B, deAbreu FR (2012a) Boron-isotopic constraints on the petrogenesis of hematitic phyllite in the southern Serra do Espinhaço, Minas Gerais, Brazil. *Lithos* 140–141:224–233
- Cabral AR, Wiedenbeck M, Rios FJ, Seabra Gomes AA Jr, Jones RD, Rocha Filho OG (2012b) Talc mineralisation associated with soft hematite ore, Gongo Soco deposit, Minas Gerais, Brazil: petrography, mineral chemistry and boron-isotope composition of tourmaline. *Mineral Deposita* 47:411–424
- Cabral AR, Zeh Z, Koglin N, Gomes AAS Jr, Viana DJ, Lehmann B (2012c) Dating the Itabira iron formation, Quadrilátero Ferrífero of Minas Gerais, Brazil at 2.65 Ga: depositional U–Pb age of zircon from a metavolcanic layer. *Prec Res* 204–205:40–45
- Cabral AR, Koglin N, Strauss H, Brätz H, Kwitko-Ribeira R (2013) Regional sulfate–hematite–sulfide zoning in the auriferous Mariana anticline, Quadrilátero Ferrífero of Minas Gerais, Brazil. *Minerium Deposita* 48 (7):805–816
- Cabral AR, Tupinambá M, Zeh A, Lehmann B, Wiedenbeck M, Brauns M, Kwitko-Ribeiro R (2017) Platiniferous gold–tourmaline aggregates in the gold–palladium belt of Minas Gerais, Brazil: implications for regional boron metasomatism. *Mineral Petrol* 111:807–819. <https://doi.org/10.1007/s00710-017-0496-0>
- Catanzaro FJ, Champion CE, Garner EL, Marinenko G, Sappenfield KM, Shields WR (1970) Boric acid: isotopic and assay standard reference materials. In: Boric Acid. US National Bur Standards Spec Pub Ser 206(17):1–70
- Cavalcanti JAD (2003) Origem dos turmalinitos auríferos da região sudeste do Quadrilátero Ferrífero-MG: evidências de campo,

- petrografia, química mineral e dados isotópicos de Nd e Sr. Unpub PhD Dissertation, Universidade Estadual de Campinas, Brazil, 192p
- Cavalcanti JAD, Xavier RP (2006) Origem dos turmalinitos auríferos da região sudeste do Quadrilátero Ferrífero—MG: geologia, petrografia, química mineral e isótopos de Nd. *Rev Bras Geoci* 36:636–647
- Chauvet A, Piantone P, Barbanson L, Nehlig P, Pedroletti I (2001) Gold deposit formation during collapse tectonics: structural, mineralogical, geochronological, and fluid inclusion constraints in the Ouro Preto gold mines, Quadrilátero Ferrífero, Brazil. *Econ Geol* 96:25–48
- Derby OA (1911) On the mineralization of the gold-bearing lode of Passagem, Minas Gerais, Brazil. *Am J Sci* 32:185–190
- Dopico CLM, Lana C, Moreira HS, Cassino LF, Alkmim FF (2017) U-Pb ages and Hf-isotopic data of detrital zircons from the late Neoproterozoic-Paleoproterozoic Minas Basin, SE Brazil. *Prec Res* 291:143–161
- Dorr JVN (1969) Physiographic, stratigraphic, and structural development of the Quadrilátero Ferrífero, Minas Gerais, Brazil. *US Geol Surv Prof Pap* 641-A:109
- Duchoslav M, Marks MAW, Drost K, McCammon C, Marschall HR, Wenzel T, Markl G (2017) Changes in tourmaline composition during magmatic and hydrothermal processes leading to tin-ore deposition: the Cornubian Batholith, SW England. *Ore Geol Rev* 83: 215–234
- Farina F, Albert C, Dopico CM, Aguilar C, Gil H, Moreira H, Hippert JP, Cutts K, Alkmim FF, Lana C (2016) The Archean-Paleoproterozoic evolution of the Quadrilátero Ferrífero (Brazil): current models and open questions. *J S AmerEarth Sci* 68:4–21
- Fleischer R, Routhier P (1973) The “consanguineous” origin of a tourmaline-bearing gold deposit: Passagem de Mariana (Brazil). *Econ Geol* 68:11–22
- Galbraith CG, Clarke DB, Trumbull RB, Wiedenbeck M (2009) Assessment of tourmaline compositions as an indicator of emerald mineralization at the Tsa da Glisza prospect, Yukon Territory, Canada. *Econ Geol* 104:713–731
- Gale A, Dalton CA, Langmuir CH, Su Y, Schilling J-G (2013) The mean composition of ocean ridge basalts. *Geochem Geophys Geosyst* 14: 489–518
- Garda GM, Schorsch JHD, Beljavskis P, Mansueto MS, Navarro MS, Mota AA (2009a) Composição química da turmalina de turmalinitos estratiformes da Mina de Passagem de Mariana, sudeste do Quadrilátero Ferrífero (MG). *Geologia USP* 9:3–22
- Garda GM, Trumbull RB, Beljavskis P, Wiedenbeck M (2009b) Boron isotope composition of tourmalinite and vein tourmalines associated with gold mineralization, Serra do Itaberaba Group, Central Ribeira Belt, SE Brazil. *Chem Geol* 264:207–220
- Garda GM, Xavier RP, Cavalcanti JAD, Trumbull RB, Wiedenbeck M (2010) Significance of compositional and boron isotope variations in tourmaline of Passagem de Mariana gold mine, Quadrilátero Ferrífero, Minas Gerais, Brazil. *Acta Miner Petrogr Abst Ser* 6:483
- Hawthorne FC, Henry DJ (1999) Classification of the minerals of the tourmaline group. *Eur J Mineral* 11:201–215
- Hazarika P, Upadhyay D, Pruseth KL (2017) Episodic tourmaline growth and re-equilibration in mica pegmatite from the Bihar mica belt, India: major- and trace-element variations under pegmatitic and hydrothermal conditions. *Geol Mag* 154:68–86
- Henry DJ, Guidotti CV (1985) Tourmaline as a petrogenetic indicator mineral: an example from the staurolite-grade metapelites of NW Maine. *Am Mineral* 70:1–15
- Henry DJ, Novák M, Hawthorne FC, Ertl A, Dutrow BL, Uher P, Pezzotta F (2011) Nomenclature of the tourmaline-super-group minerals. *Am Mineral* 96:895–913
- Hofmann AW (1988) Chemical differentiation of the Earth—the relationship between mantle, continental crust, and oceanic crust. *Earth Planet Sci Lett* 90:297–314
- Kalliomäki H, Wagner T, Fusswinkel T, Sakellaris G (2017) Major and trace element geochemistry of tourmalines from Archean orogenic gold deposits: proxies for the origin of gold mineralizing fluids? *Ore Geol Rev* 91:906–927. <https://doi.org/10.1016/j.oregeorev.2017.08.104>
- Kasemann SA, Meixner A, Erzinger J, Vieamonte JG, Alonso RN, Franz G (2004) Boron isotope composition of geothermal fluids and borate minerals from salt deposits (central Andes/NW Argentina). *J S AmerEarth Sci* 16:685–697
- Klein C, Ladeira EA (2000) Geochemistry and petrology of some Proterozoic banded iron-formations of the Quadrilátero Ferrífero, Minas Gerais, Brazil. *Econ Geol* 95:405–428
- Klemme S, Marschall HR, Jacob DE, Prowatke S, Ludwig T (2011) Trace-element partitioning and boron isotope fractionation between white mica and tourmaline. *Can Mineral* 49:165–176
- Koglin N, Zeh A, Cabral AR, Gomes AAS Jr, Corrêa Neto AV, Brunetto WJ, Galbati H (2014) Depositional age and sediment source of the auriferous Moeda Formation, Quadrilátero Ferrífero of Minas Gerais, Brazil: new constraints from U-Pb-Hf isotopes in zircon and xenotime. *Precam Res* 255:96–108
- Leeman WP, Tonarini S (2001) Boron isotopic analysis of proposed borosilicate mineral reference samples. *Geostand Newslett* 25:399–403
- Lobato LM, Ribeiro-Rodrigues LC, Vieira FWR (2001) Brazil’s premier gold province: part II. Geology and genesis of gold deposits in the Archean Rio das Velhas greenstone belt, Quadrilátero Ferrífero. *Mineral Deposita* 36:249–277
- Lüders V, Romer RL, Cabral AR, Schmidt C, Banks DA, Schneider J (2005) Genesis of itabirite-hosted Au-Pd-Pt-bearing hematite-(quartz) veins, Quadrilátero Ferrífero, Minas Gerais, Brazil: constraints from fluid inclusion infrared microthermometry, bulk crush-leach analysis and U-Pb systematics. *Mineral Deposita* 40: 289–306
- Machado N, Noce CM, Ladeira EA, Belo de Oliveira O (1992) U-Pb geochronology of Archean magmatism and metamorphism in the Quadrilátero Ferrífero, southern São Francisco craton, Brazil. *Geol Soc Am Bull* 104:1221–1227
- Marks MAW, Marschall HR, Schühle P, Guth A, Wenzel T, Jacob DE, Barth M, Mark G (2013) Trace element systematics of tourmaline in pegmatitic and hydrothermal systems from the Variscan Schwarzwald (Germany): the importance of major element composition, sector zoning, and fluid or melt composition. *Chem Geol* 344: 73–90
- Marschall HR (2018) Boron isotopes in the ocean floor realm and the mantle. In: Marschall HR, Foster GL (eds) *Advances in isotope geochemistry—boron isotopes—the fifth element*. Springer-Verlag, Heidelberg, pp 189–215
- Meyer C, Wunder B, Meixner A, Romer RL, Heinrich W (2008) Boron isotope fractionation between tourmaline and fluid: an experimental re-investigation. *Contrib Mineral Petrol* 156:259–267
- Oliveira EF, Castañeda C, Eeckhout SG, Gilmar MM, Kwitko RR, Grave E, Botelho NF (2002) Infrared and Mössbauer study of Brazilian tourmalines from different geological environments. *Am Mineral* 87:1154–1163
- Palmer MR, Slack JF (1989) Boron isotopic composition of tourmaline from massive sulfide deposits and tourmalinites. *Contrib Mineral Petrol* 103:434–451
- Redler C, Irouschek A, Jeffries T, Gieré R (2016) Origin and formation of tourmaline-rich cordierite-bearing metapelitic rocks from Alpe Sponda, central Alps (Switzerland). *J Petrol* 57:277–308
- Rudnick RL, Gao S (2014) Composition of the continental crust. In: Turekian K, Holland H (eds) *Treatise on geochemistry*, 2nd edn. Elsevier, Amsterdam, pp 1–64
- Spier CA, de Oliveira SMB, Sial AN, Rios FJ (2007) Geochemistry and genesis of the banded iron formations of the Cauê Formation, Quadrilátero Ferrífero, Minas Gerais, Brazil. *Prec Res* 152:170–206
- Taylor SR, McLennan SM (1985) The continental crust: its composition and evolution. *Blackwell Sci Publ, Oxford* 312 pp

- Teixeira W, Carneiro MA, Noce CA, Machado N, Sato K, Taylor PN (1996) Pb, Sr and Nd isotope constraints on the Archean evolution of gneissic granitoid complexes in the southern São Francisco craton, Brazil. *Precambrian Res* 78:151–164
- Trumbull RB, Slack JF (2018) Boron isotopes in the continental crust: granites, pegmatites, felsic volcanic rocks, and related ore deposits. In: Marshall HR, Foster GL (eds) *Advances in isotope geochemistry—boron isotopes—the fifth element*. Springer-Verlag, Heidelberg, pp 249–272
- Trumbull RB, Krienitz M-S, Grundmann G, Wiedenbeck M (2009) Tourmaline geochemistry and $\delta^{11}\text{B}$ variations as a guide to fluid–rock interaction in the Habachtal emerald deposit, Tauern Window, Austria. *Contrib Mineral Petrol* 157:411–427
- Trumbull RB, Slack JF, Krienitz M-S, Belkin HE, Wiedenbeck M (2011) Fluid sources and metallogenesis in the Blackbird Co–Cu–Au–Bi–Y–REE district, Idaho, U.S.A.: insights from major-element and boron isotopic compositions of tourmaline. *Can Mineral* 49:225–244
- van Hinsberg VJ (2011) Preliminary experimental data on trace-element partitioning between tourmaline and silicate melt. *Can Mineral* 49:153–163
- van Hinsberg VJ, Schumacher JC (2011) Tourmaline as a petrogenetic indicator mineral in the Haut-allier metamorphic suite, Massif Central, France. *Can Mineral* 49:177–194
- Vial DS, Duarte BP, Fuzikawa K, Vieira MBH (2007) An epigenetic origin for the Passagem de Mariana gold deposit, Quadrilátero Ferrífero, Minas Gerais, Brazil. *Ore Geol Rev* 32:596–613
- Wunder B, Meixner A, Romer RL, Wirth R, Heinrich W (2005) The geochemical cycle of boron: constraints from boron isotope partitioning experiments between mica and fluid. *Lithos* 84:206–216
- Yang S-Y, Jiang S-Y, Zhao K-D, Dai B-Z, Yang T (2015) Tourmaline as a recorder of magmatic–hydrothermal evolution: an in situ major and trace element analysis of tourmaline from the Qitianling batholith, South China. *Contrib Mineral Petrol* 170:42. <https://doi.org/10.1007/s00410-015-1195-7>